Water Resources Research

RESEARCH ARTICLE
10.1029/2023WR036059

An Electrical Parameter Characterizing Solute Heterogeneity: The Mixing Factor *M*

Alejandro Fernandez Visentini[1,2,3] **and Niklas Linde**[1]

[1]Institute of Earth Sciences, University of Lausanne, Lausanne, Switzerland, [2]French Geological Survey, Orléans, France, [3]Institute of Environmental Assessment and Water Research, Barcelona, Spain

Key Points:

- Petrophysical parameter generalizing the high-salinity limit of electrical conduction for heterogeneous fluid conductivity in porous media
- Formal expression for *M* provides framework to interpret impact of small-scale fluid conductivity heterogeneity on electrical measurements
- The mixing factor *M* depends on geostatistical properties of solute concentration fields and thus on transport characteristics

Supporting Information:

Supporting Information may be found in the online version of this article.

Correspondence to:

A. Fernandez Visentini,
afvash@cid.csic.es

Citation:

Fernandez Visentini, A., & Linde, N. (2024). An electrical parameter characterizing solute heterogeneity: The mixing factor *M*. *Water Resources Research*, *60*, e2023WR036059. https://doi.org/10.1029/2023WR036059

Received 16 AUG 2023
Accepted 3 MAY 2024

Abstract Quantitative estimates of hydrological state variables using electrical or electromagnetic geophysical methods are systematically biased by overlooked heterogeneity below the spatial scale resolved by the method. We generalize the high-salinity asymptotic limit of electrical conduction in porous media at the continuous (e.g., Darcy) scale, by introducing a new petrophysical parameter, the mixing factor *M*, which accounts for the effect of fluid conductivity heterogeneity on the equivalent electrical conductivity tensor; it is expressed in terms of the volume-average of the product of mean-removed fluid conductivity and electric fields. We investigate the behavior of *M* for static and evolving fluid conductivity scenarios. Considering 2-D ergodic log-normal random fields of fluid conductivity, we demonstrate, in absence of surface conductivity, that observing the components of the *M*-tensor allows univocally determining the variance and anisotropy of the field. Further, time-series of the *M*-tensor under diffusion-limited mixing allows distinguishing between different characteristic temporal scales of diffusion, which are directly related to the initial integral scales of the salinity field. Under advective-diffusive transport and for a pulse injection, the time-series of *M* have a strong dependence on the Péclet number. Since *M* is defined in the absence of surface conductivity, we investigate how to correct measurements for surface conductivity effects. The parameter *M* provides conceptual understanding about the impact of saline heterogeneity on electrical measurements. Further work will investigate how it can be incorporated into hydrogeophysical inverse formulations and interpretative frameworks.

Plain Language Summary Electrical and electromagnetic geophysical methods provide information about the spatio-temporal distribution of average electrical conductivity of porous media. This property is affected by the transport of electrically conductive solutes, which unfolds over a wide range of spatial scales. However, when translating electrical data into solute concentration, almost all studies to date have ignored solute heterogeneity below the averaging volume inherent to geophysical measurements or modeling, leading to unphysical results. We introduce the mixing factor *M*, an electrical parameter that links small-scale solute heterogeneity and average electrical conductivity, via a closed-form expression depending on the small-scale features of electric and solute concentration fields. We show that observation of the *M*-tensor allows recovering the variance and anisotropy of the solute field in a time-static setting. For diffusion-limited transport, the time-series of *M* help distinguishing the initial length scales of the fields, whereas for advective-diffusive transport, these data help distinguishing the Peclet number. The presented framework helps to decode information about solute heterogeneity that is contained in geoelectrical measurements, while also avoid making biased hydrological estimates. Future venues of research will investigate how to incorporate *M* in available (hydro)geophysical modeling workflows.

1. Introduction

The direct-current (DC) geophysical method aims at retrieving the spatial distribution of electrical resistivity in geological media at some given scale. The data are typically acquired using two electrode pairs: one to drive a known electrical current between two positions and another to measure the voltage between two other positions (e.g., Binley & Slater, 2020; Keller & Frischknecht, 1966). The resistance (measured voltage over injected current) is then multiplied by a geometric factor to account for measurement geometry, yielding an apparent electrical resistivity. In field settings, multiple current and electrode pairs are used to obtain many hundreds or thousands of apparent resistivity values that are subsequently inverted to derive electrical resistivity images at a resolution that varies within the tomogram. This process is often referred to as Electrical Resistivity Tomography (ERT), or time-lapse ERT, when repeating the measurement sequence to study dynamic phenomena. In this study, focusing on how saline heterogeneity affects average electrical properties, we consider as examples electrical

resistivity measurements using line electrodes that cover the pair of opposite sides of 2-D bounded domains, although our results are also valid in 3-D. For this measurement configuration, the resulting apparent conductivity (inverse of apparent resistivity) equates to the equivalent electrical conductivity σ_{eq} of the sample (e.g., Sanchez-Vila et al., 2006).

The equivalent electrical conductivity σ_{eq} of composite media, at a given scale, depends in general on both low- and high-order spatial statistics, collectively termed microstructural properties, of the averaged electrical conductivity field $\sigma(\mathbf{x})$ (e.g., Milton & Sawicki, 2003; Torquato & Haslach, 2002). For a fluid-saturated porous medium with an isolating matrix, σ_{eq} is only controlled by the microstructure of the pore space and that of $\sigma_w(\mathbf{x})$, the heterogeneous fluid electrical conductivity field residing within the pores. When $\sigma_w(\mathbf{x})$ is homogeneous and surface conductivity is ignored, σ_{eq} is solely affected by the geometry of the pore space, as expressed by the formation factor F (e.g., Archie, 1942; Johnson et al., 1986), and the constant value σ_w. A typical situation arises when $\sigma_w(\mathbf{x})$ is related to a heterogeneous and time-evolving saline concentration field $c(\mathbf{x})$ that is transported by advection and diffusion, with $\sigma_w(\mathbf{x})$ and $c(\mathbf{x})$ being related by a one-to-one relationship (e.g., Sen & Goode, 1992). In general, the time-series of σ_{eq} carry information about the time-evolution of $c(\mathbf{x})$ (e.g., Visentini et al., 2020, 2021) explaining why time-lapse ERT has been routinely applied to estimate transport characteristics of saline bodies (e.g., Binley et al., 2015). For example, time-lapse ERT has proven effective to constrain the position and approximate shape of saline plumes (e.g., Slater et al., 2000) and advective-dispersive behavior (e.g., Kemna et al., 2002; Koestel et al., 2008; Vanderborght et al., 2005), as well as dual-domain transport parameters (e.g., Day-Lewis & Singha, 2008; Singha et al., 2007).

In most such hydrogeophysical studies, the relationships established by Archie (1942) are routinely applied to transform electrical data or models (e.g., σ_{eq}-measurements or cell values of inverted electrical images) into salinity-related information (e.g., Revil et al., 2018). However, a homogeneous field $\sigma_w(\mathbf{x})$, as assumed by Archie (1942), is more the exception than the rule. Indeed, orders of magnitude variations in permeability, which greatly affect solute transport, are commonly observed in aquifers (e.g., Dentz et al., 2016; Fetter, 2018; Gelhar & Axness, 1983). This implies that $c(\mathbf{x})$ can strongly vary during transport and is seldom homogenized by molecular diffusion at usual temporal scales of observation (e.g., Berkowitz et al., 2006; Matheron & De Marsily, 1980). Thus, the assumption of a constant $\sigma_w(\mathbf{x})$ below the scale associated with electrical data, or models at the resolution of the tomograms, has been used to explain the poor recovery of spatial and temporal moments of tracer plumes from electrical monitoring (e.g., Doetsch et al., 2012; Laloy et al., 2012; Müller et al., 2010; Singha & Gorelick, 2005). Furthermore, this assumption of homogeneity implies that any information contained in σ_{eq} pertaining to the microstructure of $\sigma_w(\mathbf{x})$, and consequently $c(\mathbf{x})$, is lost.

Upscaling methodologies exist to predict σ_{eq} based on different working assumptions and microstructural properties of heterogeneous fields $\sigma(\mathbf{x})$. Popular approaches in the electrical and stochastic subsurface hydrogeology literature are perturbation (e.g., Bender & Orszag, 1999), Effective Medium Approximation (EMA) (e.g., Choy, 2015), and percolation theory (e.g., Katz & Thompson, 1986; Kirkpatrick, 1973), although other formalisms have been applied, such as the method of moments (e.g., Dykaar & Kitanidis, 1993), or devised, such as the residual flux approach (Neuman & Orr, 1993). The reader is referred to Wen and Gómez-Hernández (1996), Renard and De Marsily (1997) or Sanchez-Vila et al. (2006) for comprehensive reviews. The assumptions and workflows for each of these methodologies are different. For instance, in the perturbative approach, mostly seen in hydraulic conductivity upscaling (e.g., Dagan, 1993; Gelhar & Axness, 1983; Indelman & Abramovich, 1994; Rubin & Seong, 1994), closed-form expressions are obtained for σ_{eq} as a function of the mean, variance and integral scales of the underlying heterogeneous field $\sigma(\mathbf{x})$, the latter modeled as a spatial random function, typically log-normally distributed and first-order spatially stationary (e.g., Dagan, 1993; Gelhar & Axness, 1983; Indelman & Abramovich, 1994) or with a linear trend in the mean value (e.g., Rubin & Seong, 1994). The well-known upper and lower bounds of conductivity, consisting in the arithmetic and harmonic means of $\sigma(\mathbf{x})$, respectively, can be derived from the perturbative approach (e.g., Dagan, 1989). EMA-based approaches have been applied to model both hydraulic (e.g., Dagan, 1979; Fokker, 2001) and electrical conductivity (e.g., Bussian, 1983; Sen et al., 1981). Here, $\sigma(\mathbf{x})$ is replaced by a fictitious medium, a spatially stationary ensemble of, for instance, spherical or ellipsoidal inclusions of some conductivity that are submerged in a matrix of contrasting conductivity. By making assumptions about the interaction of the field perturbations due to the inclusions, σ_{eq} is expressed in terms of the conductivity, volume fraction and some shape measure of the inclusions (e.g., Chelidze & Gueguen, 1999; Choy, 2015). Among percolation-based approaches, which conceptualize $\sigma(\mathbf{x})$ as a pore-network, the critical path analysis (CPA) (Hunt & Sahimi, 2017; Katz & Thompson, 1986) is frequently

encountered in the hydrogeology literature (Daigle, 2016; Ewing & Hunt, 2006; Friedman & Seaton, 1998; Hunt, 2001); it assumes that σ_{eq} is controlled by a path of least resistance connecting the two sides of the domain sustaining the electrical potential (or pressure head) difference, thereby implying that most of the flow is restricted to the critical path. In its simplest version, the CPA gives σ_{eq} as the conductance of the critical path (e.g., Hunt & Sahimi, 2017).

In this study, we consider a new interpretation framework for hydrogeophysical experiments, with focus on saline transport, whereby estimations of σ_{eq} have been typically interpreted in terms of homogeneous saline fields below a given scale. To this end, we introduce a new petrophysical parameter, the mixing factor M, which quantifies the departure of σ_{eq} from its maximum attainable value, corresponding to the case where some given mass of salt is homogeneously dissolved within the porous space. In this way, we separate the electrical signatures arising from the amount of salt in the system, from its spatial configuration. In analogy with the formal definition of the formation factor (e.g., Avellaneda & Torquato, 1991), we define M for ergodic media in the absence of surface conduction and for domains with spatially constant microstructural properties, although an apparent (equivalent) M can always be measured or computed when these conditions are not met.

In Section 2, we introduce the concept of scale separation, we review the governing equations of flow and solute transport at Darcy scale, and some associated descriptors. We also review the governing equations of DC electrical conduction and the energy representation of σ_{eq} used throughout the paper. Further, we describe the problem of electrical conduction in saturated porous media and express the high-salinity asymptotic limit for σ_{eq}, leading to the formal definition of electrical textural parameters. In Section 3, we introduce our generalization of the high-salinity limit of electrical conduction in saturated porous media and the formal expression for the mixing factor M, followed by a corresponding expression of an apparent mixing factor, M^{app}, for the case where the underlying assumptions of M are not met and how to correct it. Numerical tests are presented in Section 4, a detailed discussion is provided in Section 5, and conclusions are given in Section 6.

2. Background Theory

2.1. Scale Separation

Consider a water-saturated porous medium sample that is described using two different coordinate systems (e.g., Adrian et al., 2000; Cortis et al., 2004; Wood, 2009): the small-scale coordinate $\mathbf{y}$, describing the pore space, and the large-scale coordinate $\mathbf{x}$, used to represent, for instance, the Darcy scale, where the governing flow and transport equations are considered. The sample has volume V, pore volume V_p and average porosity $\phi = V_p/V$. The pore space is filled with a heterogeneous solution consisting of some mass m of salt dissolved in denaturated water, which results in a saline concentration field $c(\mathbf{x})$ with mean value $\mu_c = m/V_p$. A 2-D view of the considered system is illustrated in Figure 1 and can represent, for instance, a saline plume.

2.2. Governing Equations of Groundwater Flow and Solute Transport

2.2.1. Groundwater Flow

For incompressible and steady-state flow in absence of sources or sinks, water mass conservation is expressed by the continuity equation for specific discharge $\mathbf{q}(\mathbf{x})$ in the following form:

$$\nabla \cdot \mathbf{q}(\mathbf{x}) = 0. \tag{1}$$

Darcy's constitutive law states

$$\mathbf{q}(\mathbf{x}) = -K(\mathbf{x})\nabla h(\mathbf{x}), \tag{2}$$

where $K(\mathbf{x})$ and $h(\mathbf{x})$ denote the hydraulic conductivity and head, respectively. Employing Equation 2 to substitute $\mathbf{q}(\mathbf{x})$ in Equation 1, the groundwater flow equation reads:

$$\nabla K(\mathbf{x}) \cdot \nabla h(\mathbf{x}) + K(\mathbf{x})\nabla^2 h(\mathbf{x}) = 0, \tag{3}$$

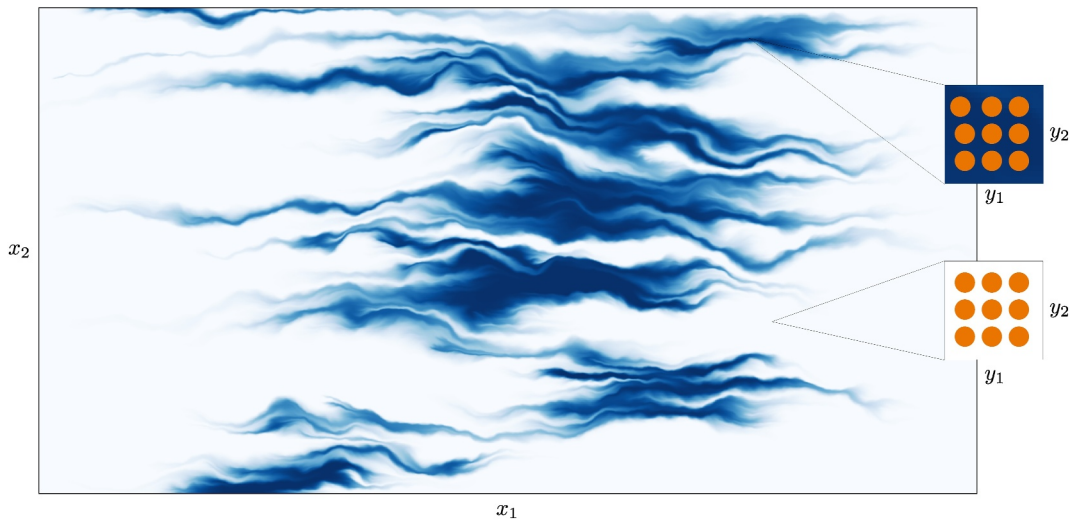

Figure 1. The large rectangle represents a heterogeneous saline field $c(\mathbf{x})$ in a saturated formation. The scale **x** (e.g., Darcy's scale) at which the salinity fluctuations are represented has well-defined porosity ϕ and is larger than the scale **y** (unresolved and not represented) at which the pore-space is described. The smaller squares at the right side represent zoomed-in views of the salinity field (i.e., at the **y**-scale, at which the salinity is assumed to be constant) at different **x**-points with (top) high and (bottom) low saline concentrations.

subject to boundary conditions. In the examples considered in this study, Equation 3 is solved numerically using the open-source finite-difference solver MODFLOW-2005 (Harbaugh, 2005).

2.2.2. Solute Transport

We model solute transport within an Eulerian framework using the Advection-Dispersion Equation (ADE):

$$\phi \frac{\partial c(\mathbf{x},\mathbf{t})}{\partial t} + \mathbf{q}(\mathbf{x}) \cdot \nabla c(\mathbf{x},t) - \nabla[\mathbf{D}(\mathbf{x}) \cdot \nabla c(\mathbf{x},t)] = 0, \tag{4}$$

where $\mathbf{D}(\mathbf{x})$ is the (local) dispersion tensor, which encompasses molecular diffusion and hydrodynamic dispersion (e.g., Bear, 1972). The molecular diffusion coefficient is set $D = 10^{-9}$ m^2 s^{-1} and the hydrodynamic dispersion coefficient is set close to zero, in order to avoid numerical errors associated to cross-dispersion terms (e.g., Yan & Valocchi, 2020). That is, we assume that no dispersivity comes from unresolved heterogeneity, which partially inhibits the spreading of the plume, particularly in the mean flow direction. Equation 4 is solved numerically using the groundwater solute transport simulator package MT3D-USGS (Bedekar et al., 2016).

The location $\alpha(t)$ of the centre of mass of a solute plume observed over V is given by the first spatial moment of $c(\mathbf{x}, t)$:

$$\alpha(t) = \int_V c(\mathbf{x},t)\mathbf{x}dV. \tag{5}$$

This expression assumes that $c(\mathbf{x}, t)$ is normalized (i.e., it satisfies $\int_V c(\mathbf{x}, t)dV = 1$).

A standard measure of the spread (or spatial extent) of a solute plume around its centre of mass is given by the second spatial moment of normalized $c(\mathbf{x}, t)$ centered at $\alpha(t)$ (e.g., Kitanidis, 1994):

$$\Delta_{ij}(t) = \int_V c(\mathbf{x},t)(x_i - \alpha_i(t))\,(x_j - \alpha_j(t))\,dV. \tag{6}$$

Solute spreading is driven by heterogeneity in $\mathbf{q}(\mathbf{x})$, which tends to segregate the solute plume into lamellar structures (e.g., Le Borgne et al., 2015) that induce concentration gradients $\nabla c(\mathbf{x}, t)$ (e.g., Kitanidis, 1994). In

contrast, molecular diffusion tends to diminish $\nabla c(\mathbf{x}, t)$ (i.e., to mix the solute) at a rate that is proportional to $\nabla c(\mathbf{x}, t)$. The global rate at which solute heterogeneity is dissipated by molecular diffusion is typically quantified by the scalar dissipation rate $\chi(t)$ (e.g., Dentz et al., 2011; Pope, 2001), which is expressed as:

$$\chi(t) = \int_V \nabla c(\mathbf{x},t) \cdot (\mathbf{D}(\mathbf{x}) \nabla c(\mathbf{x},t)) dV, \tag{7}$$

or, assuming $\mathbf{D}(\mathbf{x}) = \mathbf{I}D$ for all $\mathbf{x}$, in which $\mathbf{I}$ is the identity matrix, more simply

$$\chi(t) = D \int_V |\nabla c(\mathbf{x},t)|^2 dV. \tag{8}$$

This rate $\chi(t)$ serves also as a global measure of solute plume heterogeneity. In general, there exists a competition between spreading and mixing to, respectively, create and erase the field $\nabla c(\mathbf{x}, t)$. Such a process becomes balanced for some value of $\nabla c(\mathbf{x}, t)$ which, for a given mass of solute, is given by the Batchelor scale (e.g., Dentz et al., 2016; Villermaux, 2019).

Finally, it is useful to define the Péclet number, Pe, which measures the relative contribution to solute transport by advection and by diffusion:

$$Pe = \frac{\tau_D}{\tau_{\mathrm{ADV}}} \tag{9}$$

where τ_D and τ_{ADV} indicate characteristic diffusive and advective transport time-scales, defined as $\tau_D = l^2/D$ and $\tau_{\mathrm{ADV}} = l/\overline{v}$, with l, D and $\overline{v}$ denoting, respectively, a characteristic length of the system, the diffusion coefficient, and the mean solute velocity, the latter given as $\overline{v}_s = \overline{q}/\phi$, with $\overline{q}$ and ϕ the mean value for the specific discharge and the porosity, respectively.

2.3. DC Electrical Conduction

We first consider the governing electrical equations at the smaller scale $\mathbf{y}$. For steady-state DC conduction, and in the absence of current sources or sinks, the principle of electric charge conservation is expressed by the continuity equation for the current density $\mathbf{J}(\mathbf{y})$:

$$\nabla \cdot \mathbf{J}(\mathbf{y}) = 0. \tag{10}$$

Ohm's law relates $\mathbf{J}(\mathbf{y})$ with the electrical conductivity $\sigma(\mathbf{y})$ and the electric field $\mathbf{E}(\mathbf{y})$ via the linear relationship $\mathbf{J}(\mathbf{y}) = \sigma(\mathbf{y})\mathbf{E}(\mathbf{y})$. Adopting the quasistatic approximation, $\nabla \times \mathbf{E}(\mathbf{y}) = 0$, allows to express $\mathbf{E}(\mathbf{y}) = -\nabla U(\mathbf{y})$, where $U(\mathbf{y})$ is the electrical potential. Writing $\mathbf{J}(\mathbf{y})$ in terms of $U(\mathbf{y})$ as $\mathbf{J}(\mathbf{y}) = -\sigma(\mathbf{y})\nabla U(\mathbf{y})$ and replacing this expression into Equation 10 results in the governing Laplace equation for the electrical potentials:

$$\nabla \sigma(\mathbf{y}) \cdot \nabla U(\mathbf{y}) + \sigma(\mathbf{y}) \nabla^2 U(\mathbf{y}) = 0. \tag{11}$$

If the electrical conductivity field $\sigma(\mathbf{y})$ and boundary conditions for $U(\mathbf{y})$ are given, Equation 11 can be solved for $U(\mathbf{y})$.

The equivalent (or block-averaged) electrical conductivity $\overline{\overline{\sigma}}_{\mathrm{eq}}$ of the considered domain, at a given scale, can be defined through an averaged Ohm's law over its volume V (e.g., Sanchez-Vila et al., 2006):

$$\overline{\mathbf{J}} = -\overline{\overline{\sigma}}_{\mathrm{eq}} \int_{\mathrm{V}} \nabla U(\mathbf{y}) dV, \tag{12}$$

where $\overline{\mathbf{J}}$ designates the block-averaged current density $\mathbf{J}$. For media that behaves anisotropically at the scale of V, $\overline{\overline{\sigma}}_{\mathrm{eq}}$ is in general a 3×3 second-rank tensor. If the conductivity measurement direction is coincident with the principal directions of heterogeneity, then the tensor becomes diagonal. We will assume in the following that we

are in such a setting and, to simplify the notation, write simply σ_{eq}, while distinguishing between scalar and tensorial quantities from the context.

2.4. Electrical Textural Parameters in Porous Media

2.4.1. Energy Representation of the Equivalent Electrical Conductivity

Let us now cover two opposite faces of a cubic sample with a pair of sheet electrodes and impose an electrical potential difference ΔU along the x_1-direction (we denote the second and third directions by x_2 and x_3, respectively). This drives an electrical current I, equal to the integral of the flux of $\mathbf{J}(\mathbf{y})$ across any surface separating the injection electrodes. The power dissipated by the sample in the form of Joule's heat is given by $I\Delta U$. Applying Ohm's law we can express it as $\Sigma\Delta U^2$, with Σ the conductance (in S) of the sample, in turn given as $\Sigma = \sigma_{eq}L$, where σ_{eq} and L designate the equivalent electrical conductivity and side length of the cube, respectively. We can further express the power in terms of the modulus of the applied electric field $\mathbf{E}_0$, $E_0 \equiv -\Delta U/L$ and σ_{eq} as $VE_0^2\sigma_{eq}$. Analogously, the power dissipated locally at the point $\mathbf{y}$ is given by the product $\mathbf{E}(\mathbf{y}) \cdot \mathbf{J}(\mathbf{y})$. Again, using Ohm's law we can express $\mathbf{E}(\mathbf{y}) \cdot \mathbf{J}(\mathbf{y}) = \mathbf{E}(\mathbf{y}) \cdot \sigma(\mathbf{y})\mathbf{E}(\mathbf{y})$. This quantity, integrated over V, must be identical to $VE_0^2\sigma_{eq}$ due to energy conservation. That is:

$$\sigma_{eq} = \frac{1}{V}\int_V \mathbf{e}(\mathbf{y}) \cdot \sigma(\mathbf{y})\mathbf{e}(\mathbf{y})dV, \tag{13}$$

which gives the energy representation of σ_{eq} (e.g., Torquato & Haslach, 2002) with the normalized electric field $\mathbf{e}(\mathbf{y})$, given by $\mathbf{e}(\mathbf{y}) = \mathbf{E}(\mathbf{y})/E_0$. By imposing a no current flux condition on the remaining boundaries of the sample as done here, the net current that would flow perpendicularly to the direction of the imposed electric field is suppressed. Consequently, one obtains an approximation of σ_{eq} (e.g., Pollock & Cirpka, 2012) except if measuring in the principal directions of the electrical conductivity field as assumed herein. The energy representation of effective properties has been previously applied for both electrical (e.g., Bernabé & Revil, 1995) and hydraulic (e.g., Dagan, 1993) conductivity upscaling.

2.4.2. Effective Electrical Conductivity in Presence of Surface Conductivity

We are concerned with the case where $\sigma(\mathbf{y})$ describes the electrical conductivity of porous media that exhibit surface conduction and contains a heterogeneous scalar fluid electrical conductivity field $\sigma_w(\mathbf{y})$, the latter resulting from a heterogeneous saline concentration field $c(\mathbf{y})$ (e.g., Sen & Goode, 1992). Surface conductivity is assumed to originate from a thin electrical double layer coating the surface of the insulating grains (e.g., Revil et al., 2018). The conductivity field $\sigma(\mathbf{y})$ within the sample is then given by $\sigma(\mathbf{y}) = \sigma_w(\mathbf{y})\Phi(\mathbf{y}) + \sigma_s(\mathbf{y}^I)$, where the indicator function $\Phi(\mathbf{y})$ describes the geometry of the porous medium, taking values of zero and one in the matrix and pore space, respectively, and the surface conductivity contribution $\sigma_s(\mathbf{y}^I)$, given by $\sigma_s(\mathbf{y}^I) = \int_V \sigma_s(\mathbf{y})\delta(\mathbf{y} - \mathbf{y}^I)$ dV, is non-zero only at the water-mineral interface located at the points $\mathbf{y}^I$, with $\delta(\mathbf{y} - \mathbf{y}^I)$ denoting the delta distribution. After removing the isolating matrix from the integration and separating the bulk water and surface conductivity contributions, Equation 13 reads

$$\sigma_{eq} = \frac{1}{V}\left[\int_{V_p} \mathbf{e}(\mathbf{y}) \cdot \sigma_w(\mathbf{y})\mathbf{e}(\mathbf{y})dV_p + \int_{V_p} \mathbf{e}(\mathbf{y}^I) \cdot \sigma_s(\mathbf{y}^I)\,\mathbf{e}(\mathbf{y}^I)\,dV_p\right], \tag{14}$$

where the two terms of Equation 14 are dependent since $\mathbf{e}(\mathbf{y})$ depends on both $\sigma_w(\mathbf{y})$ and $\sigma_s(\mathbf{y}^I)$ for any $\mathbf{y}$.

2.4.3. The Formation Factor F

In the simplest case, $\sigma_w(\mathbf{y}) \equiv \mu_{\sigma_w}$ and $\sigma_s(\mathbf{y}^I) \equiv 0$, that is, bulk water and surface electrical conductivity are constant and zero, respectively. Equation 14 simplifies to:

$$\sigma_{eq} = \frac{\mu_{\sigma_w}}{F}, \tag{15}$$

where F $(-)$ designates the formation factor (Archie, 1942; Avellaneda & Torquato, 1991), defined for ergodic media as

$$\frac{1}{F} = \frac{1}{V}\int_{V_p} \mathbf{e}\cdot\mathbf{e}dV_p. \tag{16}$$

The right-hand side (RHS) of Equation 16 expresses a weighted average over the pore space, where the weights $\mathbf{e}(\mathbf{y})\cdot\mathbf{e}(\mathbf{y})$ correspond to the local dissipated power, divided by the electrical conductivity. Thus, 1/F represents an electrically connected porosity, thereby, encoding the relationship between the spatial distribution of the pore space $\Phi(\mathbf{y})$ and σ_{eq}. The formation factor F is an intrinsic property of the porous medium (e.g., Avellaneda & Torquato, 1991; Bernabé & Revil, 1995; Johnson et al., 1986).

2.4.4. High-Salinity Asymptotic Limit

If $\sigma_w(\mathbf{y}) \equiv \mu_{\sigma_w}$ and $\sigma_s\left(\mathbf{y}^I\right) \equiv \mu_{\sigma_s}$, with μ_{σ_s} being small compared to μ_{σ_w}, then the electric field is mainly controlled by bulk water conduction, implying that the additional dissipated power appearing due to surface conduction can be approximated by the interaction between μ_{σ_s} and the electric field that would exist in the absence of surface conduction. This leads to the so-called high-salinity asymptotic limit expression for σ_{eq}, which reads

$$\sigma_{\text{eq}} = \frac{\mu_{\sigma_w}}{F}\left(1 + \frac{2}{\Lambda}\frac{\mu_{\Sigma_s}}{\mu_{\sigma_w}}\right), \tag{17}$$

where μ_{σ_s} is expressed in terms of the conductance of the electrical double layer, μ_{Σ_s} (in S), as $\mu_{\sigma_s} = 2\mu_{\Sigma_s}/F\Lambda$ and Λ (in m) is defined as (Johnson et al., 1986):

$$\frac{2}{\Lambda} = \frac{\int_S \mathbf{e}\cdot\mathbf{e}dS}{\int_{V_p}\mathbf{e}\cdot\mathbf{e}dV_p}. \tag{18}$$

The parameter Λ is another intrinsic property of the porous medium and represents an (electrical) effective pore radius (e.g., Avellaneda & Torquato, 1991; Bernabé & Revil, 1995; Johnson et al., 1986; Revil & Cathles, 1999; Revil et al., 2018). Equation 18 expresses an electrically weighted surface-to-pore-volume ratio, where, again, the weights are given by the local dissipated power divided by the electrical conductivity. For completeness, we include a short derivation of the high-salinity asymptotic limit (Equation 17) in Supporting Information S1 of this article.

3. The Mixing Factor *M*

We introduce now a new petrophysical parameter, the mixing factor M, which can be used to generalize Equation 17 for the case of heterogeneous fluid conductivity $\sigma_w(\mathbf{x})$, and hence salinity $c(\mathbf{x})$, at the continuous scale $\mathbf{x}$. Its formal derivation is given in Appendix A.

3.1. Generalization of the High-Salinity Asymptotic Limit

We start by expressing the conductivity field $\sigma(\mathbf{x})$ as:

$$\sigma(\mathbf{x}) = \frac{\mu_{\sigma_w} + \sigma'_w(\mathbf{x})}{F} + \mu_{\sigma_s}, \tag{19}$$

that is, using a petrophysical relationship of the form of Equation 17, but replacing μ_{σ_w} by $\sigma_w(\mathbf{x}) = \mu_{\sigma_w} + \sigma'_w(\mathbf{x})$ (i.e., a mean value plus a spatially variable fluid conductivity fluctuation). This expression is defined in the high-salinity limit, which amounts to assuming that the first right-hand term of Equation 19 is much larger than the second term, for all $\mathbf{x}$. A spatially constant F and μ_{σ_s} are also assumed. Substituting Equation 19 into Equation 13, assuming that $\sigma'_w(\mathbf{x})$ is ergodic (e.g., Torquato & Haslach, 2002) and isotropic at the larger sample

scale and that equivalent conductivity is measured along the x_1-direction, we arrive after some manipulations (see Appendix A) at:

$$\sigma_{\text{eq}} = \frac{\mu_{\sigma_w}}{FM} + \mu_{\sigma_s}, \tag{20}$$

which is a generalized form of the high-salinity asymptotic limit, with the mixing factor M defined in the absence of surface conductivity as:

$$\frac{1}{M} = 1 + \frac{1}{\mu_{\sigma_w} V} \int_V \sigma'_w e'_{x_1} dV, \tag{21}$$

where $e'_{x_1}(\mathbf{x})$ is the x_1-component of the normalized secondary electric field $\mathbf{e}'(\mathbf{x})$ (Section 2.4.1). Further, if we assign $\mu_{\sigma_s} = 2\mu_{\Sigma_s}/\Lambda F$, we obtain:

$$\sigma_{\text{eq}} = \frac{\mu_{\sigma_w}}{F}\left(\frac{1}{M} + \frac{2}{\Lambda}\frac{\mu_{\Sigma_s}}{\mu_{\sigma_w}}\right), \tag{22}$$

which is a generalized form of the expression by Johnson et al. (1986).

The integral in Equation 21 expresses a weighted average of $\sigma'_w(\mathbf{x})$, where the weights $e'_{x_1}(\mathbf{x})$ are determined by the spatial statistics of $\sigma'_w(\mathbf{x})$, thereby highlighting the non-linearity of conductivity averaging for non-constant $\sigma_w(\mathbf{x})$. It is always non-positive, and non-zero as soon as $\sigma_w(\mathbf{x})$ develops gradients with a parallel component to the measurement direction. The inverse of M, $1/M$, ranges within (0, 1): as $\sigma_w(\mathbf{x})$ becomes more homogeneous (i.e., $\sigma'_w \to 0$) or else, laminated parallel to x_1, then $e'_{x_1}(\mathbf{x}) \to 0$ and $1/M \to 1$, thereby approaching the maximum attainable value of σ_{eq}, for given values of μ_{σ_w} and F, that is, $\sigma_{\text{A}} = \mu_{\sigma_w}/F$ if neglecting surface conductivity, corresponding to the case where $\sigma_w(\mathbf{x})$ is (trivially) averaged arithmetically. As $\sigma_w(\mathbf{x})$ becomes more heterogeneous and structured perpendicular to x_1, then $1/M \to 0$.

Assuming zero surface conductivity, Equation 20 reduces to:

$$\sigma_{\text{eq}} = \frac{\mu_{\sigma_w}}{FM}, \tag{23}$$

which is a generalized form of the petrophysical relationship (Equation 15) that is most typically used for interpretations in electrical hydrogeophysical studies.

If $\sigma_w(\mathbf{x})$ renders the sample electrically anisotropic, then both the equivalent electrical conductivity and the mixing factor become tensors $\overline{\overline{\sigma}}_{\text{eq}}$ and $\overline{\overline{M}}$, respectively, and we can write Equation 20 more generally as:

$$\overline{\overline{\sigma}}_{\text{eq}} = \frac{\mu_{\sigma_w}}{F}\left(\overline{\overline{M}}^{-1} + \mu_{\sigma_s}\right). \tag{24}$$

with $\overline{\overline{M}}^{-1}$ given as

$$\overline{\overline{M}}^{-1} = \mathbf{I} + \frac{1}{\mu_{\sigma_w} V}\begin{bmatrix} \int_V \sigma'_w e'_{x_1} dV & 0 & 0 \\ 0 & \int_V \sigma'_w e'_{x_2} dV & 0 \\ 0 & 0 & \int_V \sigma'_w e'_{x_3} dV \end{bmatrix}, \tag{25}$$

where $e'_{x_2}(\mathbf{x})$ and $e'_{x_3}(\mathbf{x})$ denote the x_2- and x_3-components, respectively, of normalized secondary electric fields arising when the conductivity measurement direction is either aligned with the x_2- or x_3-direction. Equation 25

assumes that the axes of anisotropy are aligned with the x_1- x_2- and x_3-directions. In the general case, the off-diagonal elements are non-zero.

3.2. Estimating M From Electrical Measurements

The mixing factor M (Equation 21) is formally defined for (a) an ergodic fluid conductivity field $\sigma_w(\mathbf{x})$, (b) constant formation factor F and (c) zero surface conductivity μ_{σ_s}. Regardless of whether these assumptions are met or not, an apparent mixing factor, M^{app}, can always be measured as follows:

$$M^{\text{app}} = \frac{\sigma_{\text{A}}}{\sigma_{\text{eq}}}, \tag{26}$$

where σ_{A} and σ_{eq} designate the electrical conductivities of the sample when $\sigma_w(\mathbf{x})$ is homogeneous and heterogeneous, respectively.

3.2.1. Formal Expression for M^{app}

It is straightforward to obtain a formal expression for the apparent mixing factor M^{app}. For this, we decompose both $\sigma_w(\mathbf{x})$ and $F(\mathbf{x})$ as the sum of their mean and fluctuating parts, that is, $F(\mathbf{x}) = \overline{F} + F'(\mathbf{x})$ and $\sigma_w(\mathbf{x}) = \mu_{\sigma_w} + \sigma'_w(\mathbf{x})$, to express $\sigma(\mathbf{x})$ as (similarly as in Equation 19):

$$\sigma(\mathbf{x}) = \frac{\mu_{\sigma_w}}{\overline{F}}\left[\frac{1 + \sigma'_w(\mathbf{x})/\mu_{\sigma_w}}{1 + F'(\mathbf{x})/\overline{F}} + \frac{\overline{F}}{\mu_{\sigma_w}}\mu_{\sigma_s}\right]. \tag{27}$$

Substituting Equation 27 into Equation 13 and factorizing $\mu_{\sigma_w}/\overline{F}$ out of the integral, we obtain:

$$\sigma_{\text{eq}} = \frac{\mu_{\sigma_w}}{\overline{F} M^{\text{app}}}. \tag{28}$$

with M^{app} defined as:

$$\frac{1}{M^{\text{app}}} = \frac{1}{V}\int_V \mathbf{e}\cdot\mathbf{e}\left[\frac{1 + \sigma'_w(\mathbf{x})/\mu_{\sigma_w}}{1 + F'(\mathbf{x})/\overline{F}} + \frac{\overline{F}}{\mu_{\sigma_w}}\mu_{\sigma_s}\right] dV. \tag{29}$$

This expression assumes a constant surface conductivity μ_{σ_s} of arbitrary magnitude.

3.2.2. Correcting M^{app} for Surface Conductivity

For the case of constant formation factor, a first-order correction for non-zero surface conductivity, valid in the high-salinity limit, can be implemented by subtracting μ_{σ_s} from the measured responses σ_{A} and σ_{eq}:

$$M \approx M^{\text{corr}} = \frac{\sigma_{\text{A}} - \mu_{\sigma_s}}{\sigma_{\text{eq}} - \mu_{\sigma_s}}. \tag{30}$$

As surface conductivity increases, M^{app} (Equation 26) becomes increasingly smaller than M as the influences of heterogeneity and structures of $\sigma_w(\mathbf{x})$ on σ_{eq} become less pronounced. This can be seen by writing the governing Laplace equation for the electrical potential (Equation 11) with $\sigma(\mathbf{x}) = \left(\mu_{\sigma_w} + \sigma'_w(\mathbf{x})\right)/F + \mu_{\sigma_s}$. Distributing the operator ∇, and dividing Equation 11 by μ_{σ_s}, one gets

$$\nabla\frac{\sigma'_w(\mathbf{x})}{F\mu_{\sigma_s}}\nabla U(\mathbf{x}) + \left(\frac{\mu_w + \sigma'_w(\mathbf{x})}{F\mu_{\sigma_s}} + 1\right)\nabla^2 U(\mathbf{x}) = 0. \tag{31}$$

Taking $\mu_{\sigma_s} \to \infty$, one recovers the Laplace equation for homogeneous media of conductivity μ_{σ_s}. In other words, as μ_{σ_s} increases, the surface conductivity allows the current to bypass obstacles of low salinity in $\sigma_w(\mathbf{x})$.

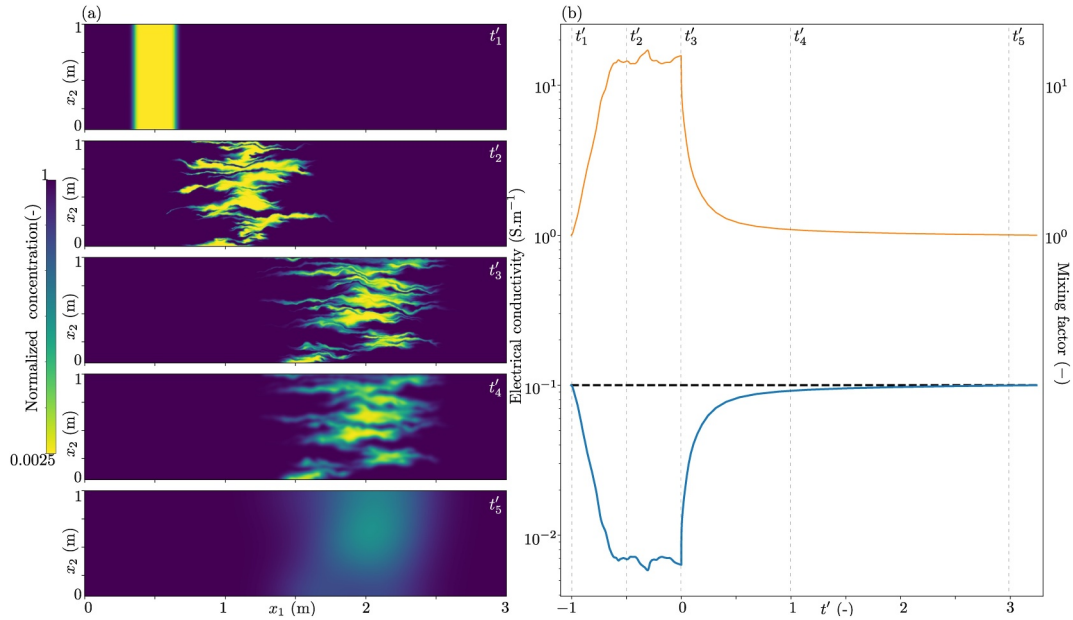

Figure 2. (a) A saline tracer is injected at time t'_1 to create a time-evolving and mass-conservative saline concentration field $c(\mathbf{x})$, which induces a fluid conductivity field $\sigma_w(\mathbf{x})$ with fixed arithmetic mean $\mu_{\sigma_w} = 1\ \mathrm{Sm}^{-1}$ and ratio of 400 between the tracer and background fluid conductivities. The tracer is transported at a high Péclet number $Pe = 1{,}000$ until t'_3, when the flow field is switched off and the tracer is let to diffuse until time t'_5. The represented $c(\mathbf{x})$-fields are normalized by the maximum concentration. (b) Arithmetic mean of fluid conductivity divided by the formation factor, σ_A (black dashed line), equivalent electrical conductivity σ_{eq} measured along the x_2-direction (blue line) and the apparent mixing factor M^{app} measured along the same direction (orange line). The underlying hydraulic conductivity is log-normally distributed, with exponential covariance, variance $\sigma_Y^2 = 1$ and integral scales in the x_1- and x_2-directions of $I_{x_1} = 0.1$ m and $I_{x_2} = 0.02$ m, respectively. The formation factor F and surface conductivity μ_{σ_s} are assumed constant and equal to 10 and 0 S m^{-1}, respectively. The represented dimensionless time t' results from normalizing the time by advective and diffusive characteristic transport time-scales, before and after switching off the injection at t'_3, respectively. The black vertical dashed lines mark the dimensionless times corresponding to the snapshots of the represented normalized saline concentration fields.

4. Numerical Tests

4.1. Interpretation of *M*

In electrically monitored saline tracer tests, the typical approach to interpret the results (e.g., Cassiani et al., 2006; Kemna et al., 2002; Müller et al., 2010; Singha & Gorelick, 2005) is to rely on an expression such as Equation 15 to estimate the mean saline concentration μ_c within the sample, by measuring or inferring σ_{eq}, assuming knowledge of F and zero surface conductivity. This approach is only meaningful when the saline field is homogeneous (i.e., completely mixed) or exhibits lamination parallel to the conductivity measurement direction. In such case, the interstitial fluid electrical conductivity trivially behaves as an additive property and the observable apparent fluid conductivity σ_w^{app} (obtained as $\sigma_{eq}F$) equates μ_{σ_w}. This establishes a link between σ_w^{app} and μ_c, via a simple transformation (e.g., Sen & Goode, 1992). However, as $\sigma_w(\mathbf{x})$ departs from homogeneity (or a layered field), σ_w^{app} becomes smaller than μ_{σ_w} and then μ_c is no longer directly accessible through σ_w^{app}. Consequently, it becomes difficult to assign a clear meaning to σ_w^{app} even in the absence of surface conductivity, except if making the questionable assumption that deviations from homogeneity have a negligible effect on the results.

In general, $1/M$ evolves in response to the evolution of $\sigma_w(\mathbf{x})$, which in turn is governed by the spreading and mixing dynamics of the solute field $c(\mathbf{x})$. This is illustrated in Figure 2. A steady-state flow field is established within a 2-D sample in absence of surface conductivity, and a saline tracer is injected and transported at high Péclet number in the x_1-direction until the tracer develops significant concentration gradients along the x_2-direction (see snapshots at times t'_1, t'_2 and t'_3 in Figure 2a). The flow field is then stopped and the tracer is let to diffuse until the gradients have practically vanished (snapshot at time t'_5 in Figure 2a). Meanwhile, σ_{eq} is measured

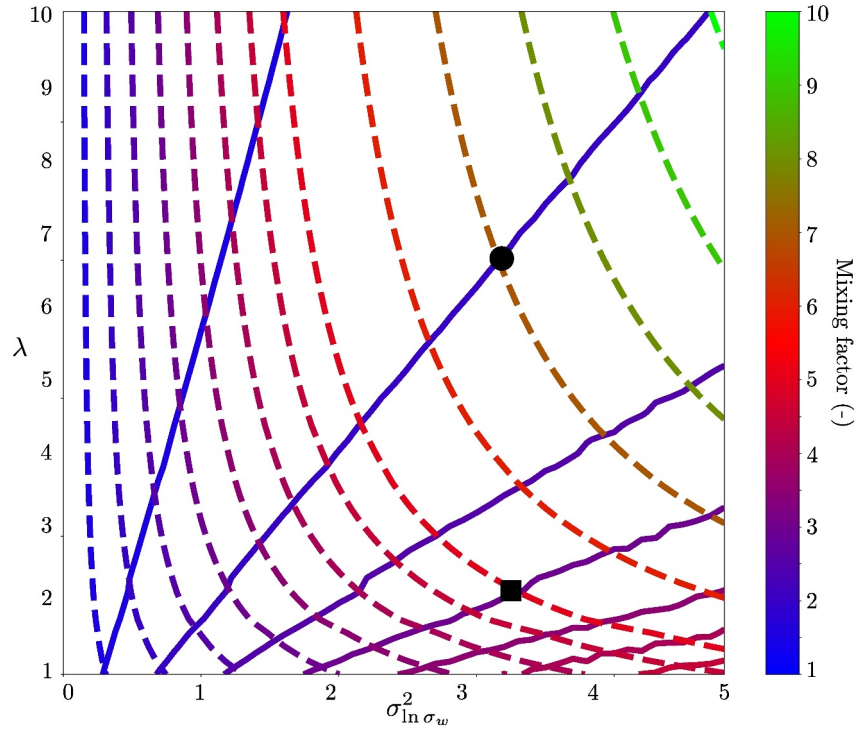

Figure 3. Contour plots of (solid lines) M_{x_1} and (dashed lines) M_{x_2} as a function of the variance $\sigma^2_{\ln\sigma_w}$ and anisotropy λ of ergodic log-normally distributed electrical fluid conductivity fields $\sigma_w(\mathbf{x})$ with exponential covariance structure. Both M_{x_1} and M_{x_2} increase with $\sigma^2_{\ln\sigma_w}$, but M_{x_1} decreases with λ whereas M_{x_2} increases with this parameter. For instance, the coordinates $(\sigma^2_{\ln\sigma_w},\lambda) = (3.4,2)$ map to $(M_{x_1},M_{x_2}) = (3,5)$ (black square), whereas $(\sigma^2_{\ln\sigma_w},\lambda) = (3.4,6.75)$ map to $(M_{x_1},M_{x_2}) = (1.5,7.5)$ (black circle).

along the x_2-direction (Figure 2b). It is readily seen that σ_{eq} increasingly departs from $\sigma_{\text{A}} = \mu_{\sigma_w}/F$ when the tracer starts to develop structures, until time t'_3. As soon as the flow-field is shut-off, σ_{eq} starts to increase, reaching again μ_{σ_w}/F at time t'_5. The mass within the sample (i.e., μ_c) remains constant, implying that σ_{eq} evolves due to structural changes in $\sigma_w(\mathbf{x})$, captured by M^{app}. In this simple example, we find that equating σ_w^{app} with μ_{σ_w} leads to an underestimation of μ_c by a factor larger than 15, or equivalently, M^{app} is larger than 15. This demonstrates that unresolved heterogeneity in the tracer (or contaminant) distribution is a likely cause for the ubiquitous and well-recognized problem of apparent mass loss when interpreting time-lapse ERT tomograms. Note that in this illustrative example used to build intuition, the salinity fields are not ergodic and hence we are observing M^{app} and not M.

4.2. Information Content of the Mixing Factor M

We now assess the sensitivity of the mixing factors M_{x_1} and M_{x_2} to parameters describing the heterogeneity and temporal evolution of 2-D saline concentration $c(\mathbf{x})$ and fluid electrical conductivity $\sigma_w(\mathbf{x})$. Since $c(\mathbf{x})$ and $\sigma_w(\mathbf{x})$ can be linked by a one-to-one mapping (e.g., Sen & Goode, 1992), we will consider these quantities interchangeably and cite one or another, depending on context.

4.2.1. Static Setting

In the absence of surface conductivity, we first demonstrate the ability of M_{x_1} and M_{x_2} to resolve the variance $\sigma^2_{\ln\sigma_w}$ and anisotropy λ of ergodic log-normal $\sigma_w(\mathbf{x})$-fields with exponential covariance structure (e.g., Rubin, 2003). The mean value and integral scale along x_2 are set as $\mu_{\sigma_w} = 1\ \text{Sm}^{-1}$ and I_{x_2}. The formation factor is set and $F = 10$. A contour plot of M_{x_1} and M_{x_2} as a function of these parameters is presented in Figure 3.

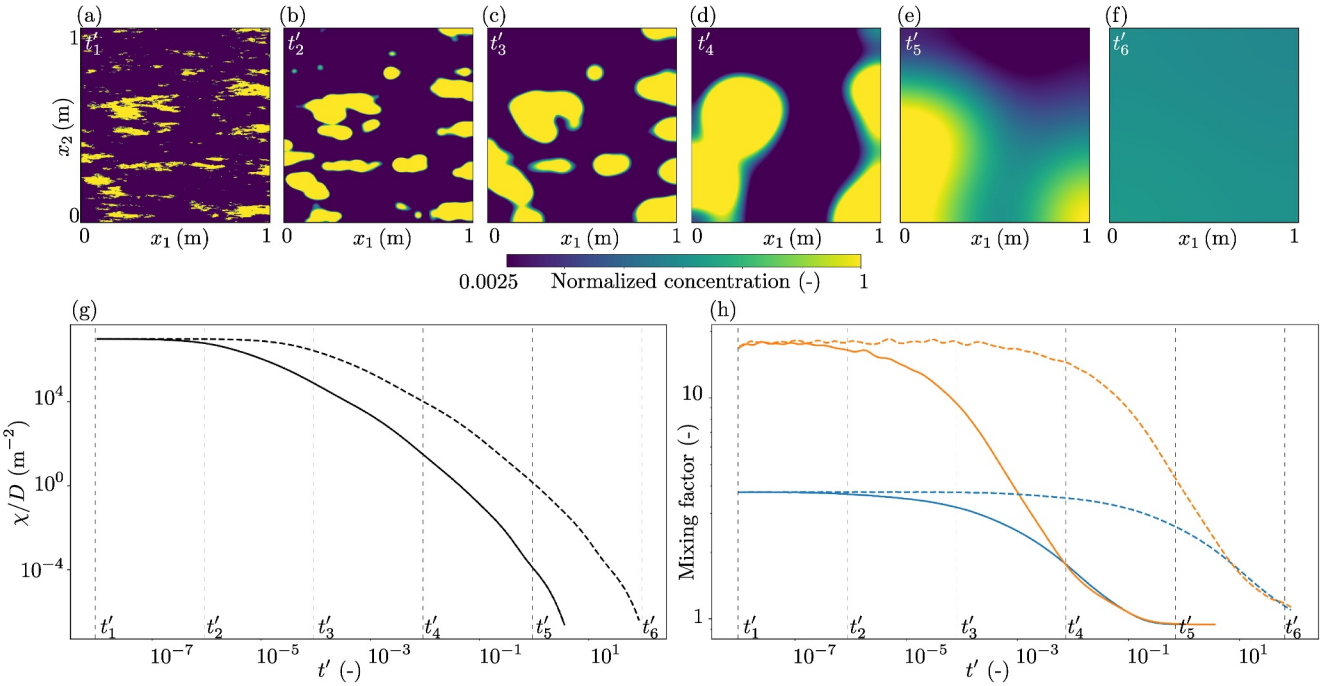

Figure 4. Electrical monitoring of the diffusion-limited mixing of two different saline fields $c(\mathbf{x})$ that at the initial time differ only in terms of their scale (see main text). (a)–(f) Evolution of $c(\mathbf{x})$ with initial integral scale $I_{x_2} = 0.02$ m (not shown for $I_{x_2} = 1$ m, as it is qualitatively identical). The diffusion coefficient for both tests is set to $D = 10^{-9}$ m^2 s^{-1}. (g) Scalar dissipation rates normalized by D for the homogenization process corresponding to $c(\mathbf{x})$-field with initial I_{x_2} equal to (solid line) $I_{x_2} = 0.02$ m and (dashed line) $I_{x_2} = 1$ m. (h) mixing factors (blue) $M^{\text{app}}_{x_1}$ and (orange) $M^{\text{app}}_{x_2}$ in the x_1- and x_2-directions, respectively, for $c(\mathbf{x})$-field with initial integral scale (solid line) $I_{x_2} = 0.02$ m and (dashed line) $I_{x_2} = 1$ m.

The intersection of the M_{x_1}- and M_{x_2}-contours shown in Figure 3 indicates that, in the absence of noise in the electrical data, a given pair of M_{x_1}- and M_{x_2}-values maps univocally to a corresponding pair $\left[\sigma^2_{\ln\sigma_w}, \lambda\right]$. Both M_{x_1} and M_{x_2} increase with the variance of the log-electrical fluid conductivity fields $\sigma^2_{\ln\sigma_w}$. For a given variance, M_{x_1} decreases with λ whereas M_{x_2} increases. As λ increases, the electrical current pathways along the x_1-and x_2-directions become less or more tortuous, respectively.

4.2.2. Diffusion-Limited Mixing

We now consider two heterogeneous $c(\mathbf{x})$-fields of the same type as in Section 4.2 that are let to diffuse. At the initial time, the two $c(\mathbf{x})$-fields have a log-normal distribution, with exponential covariance structure, mean $\mu_c = 1$ g l^{-1}, log-variance of $\sigma^2_{\ln c} = 5$ and anisotropy of $\lambda = 5$. They only differ by their integral scale I_{x_2} along the x_2-direction, which is set as 0.02 and 0.1 m for the smaller and larger field, respectively. The chosen molecular diffusion coefficient ($D = 10^{-9}$ m^2 s^{-1}, Section 2.2.2), leads to diffusion time-scales τ_D $\left(:= I^2_{x_2}/D\right)$ of, respectively, 4×10^5 s and 1×10^7 s. The homogenization of the smaller field is illustrated in Figures 4a–4f and the mixing evolution is quantified by the scalar dissipation rate, normalized by D, χ/D (Section 2.2; dashed line in Figure 4g). It starts and finishes the experiment with values of $\sim 10^6$ and $\sim 10^{-6}$ m^{-2}, respectively, indicating a large decrease of solute concentration gradients over time. The more efficient mixing of the smaller field is evidenced by the faster decay of the corresponding time-series of χ/D (solid line in Figure 4g).

The time-series of $M^{\text{app}}_{x_1}$ and $M^{\text{app}}_{x_2}$ are plotted in Figure 4h. Note that we observe M^{app} and not M, since the underlying fluid conductivity is not ergodic. At the initial times, $M^{\text{app}}_{x_2}$ is $\sim$6 times larger than $M^{\text{app}}_{x_1}$, which is expected, given the anisotropy of the field. As the mixing progresses and the heterogeneity is erased, both $M^{\text{app}}_{x_1}$ and $M^{\text{app}}_{x_2}$ converge to a value of 1. Analogously to the pair of χ/D-curves, the $M^{\text{app}}_{x_1}$ and $M^{\text{app}}_{x_2}$ time-series corresponding to the smaller field decay faster than for the larger field (dashed lines in Figure 4h), which indicates sensitivity of the M^{app} time-series to the characteristic diffusion time-scale associated to these two homogenization processes.

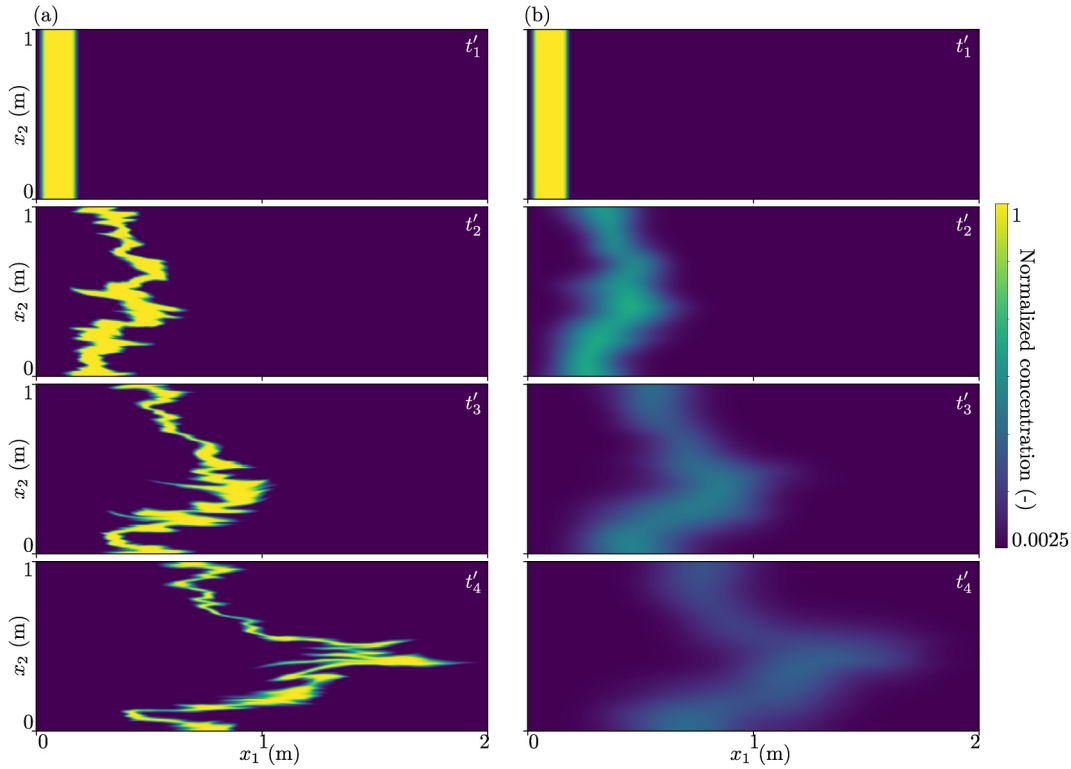

Figure 5. Two saline tracer tests performed at Péclet numbers of (a) 1,000 and (b) 1. The tracer injection starts at t'_1 and induces a fluid conductivity field $\sigma_w(\mathbf{x})$ with fixed arithmetic mean $\mu_{\sigma_w} = 1\ \mathrm{Sm}^{-1}$ and ratio of 400 between the tracer and background fluid conductivities. The underlying hydraulic conductivity is log-normally distributed, with exponential covariance, variance $\sigma^2_Y = 1$ and integral scales in the x_1- and x_2-directions of $I_{x_1} = 0.1$ m and $I_{x_2} = 0.2$ m, respectively. The formation factor F and surface conductivity μ_{σ_s} are assumed constant and equal to 10 and 0 S m^{-1}, respectively. The presented fields correspond to saline concentration fields normalized by their maximum value. The dimensionless time t' results from normalizing the time by corresponding advective transport time-scales.

4.2.3. Diffusion and Advection

We consider now the temporal evolution of $M^{\mathrm{app}}_{x_1}$ and $M^{\mathrm{app}}_{x_2}$ for two tracer tests that are performed at Péclet numbers of 1,000 (Figure 5a) and 1 (Figure 5b). Note the measurements correspond again to apparent mixing factors M^{app}, since the salinity field $c(\mathbf{x})$ is non-ergodic (Section 3.2).

In Figure 6 we show the temporal evolution of the normalized second-central moment in direction x_1, $\Delta_{x_1x_1}$ (Equation 6), the normalized scalar dissipation rate χ/D, and measured mixing factors $M^{\mathrm{app}}_{x_1}$ and $M^{\mathrm{app}}_{x_2}$ for the two tracer tests. The time vectors are normalized by the corresponding characteristic advective transport time-scales $\tau_{\mathrm{ADV}} = L/\overline{v}$ (Section 2.2.2) that differ by a factor of 1,000 due to the different mean flow velocities along the x_1-direction, with L taken as the length of the domain in the x_1-direction. This results in synchronized time-scales that we denote simply by t'.

The temporal evolution of $\Delta_{x_1x_1}$ is very similar for the fast and slow tests (Figure 6a), with $\Delta_{x_1x_1}$ increasing over approximately two orders of magnitude. This is expected, since we have set a hydrodynamic dispersion coefficient close to zero and, in addition, $\Delta_{x_1x_1}$ depends on the mean velocity of the plume and variance of the permeability field (e.g., Gelhar & Axness, 1983), which are identical for both cases. $\Delta_{x_1x_1}$ is slightly larger for the slow tracer test (orange curve) because diffusion has more time to spread the tracer horizontally. On the contrary, the mixing evolution presents marked differences between the two tracer tests (Figure 6b). For the fast tracer test (blue curve), χ/D increases over one order of magnitude, first sharply at the initial times and then slowly, whereas for the slow tracer test (orange curve), χ/D decays over two orders of magnitude. This behavior is expected, since for the test with a high Péclet number, the rate of creation of concentration gradients due to flow heterogeneity is

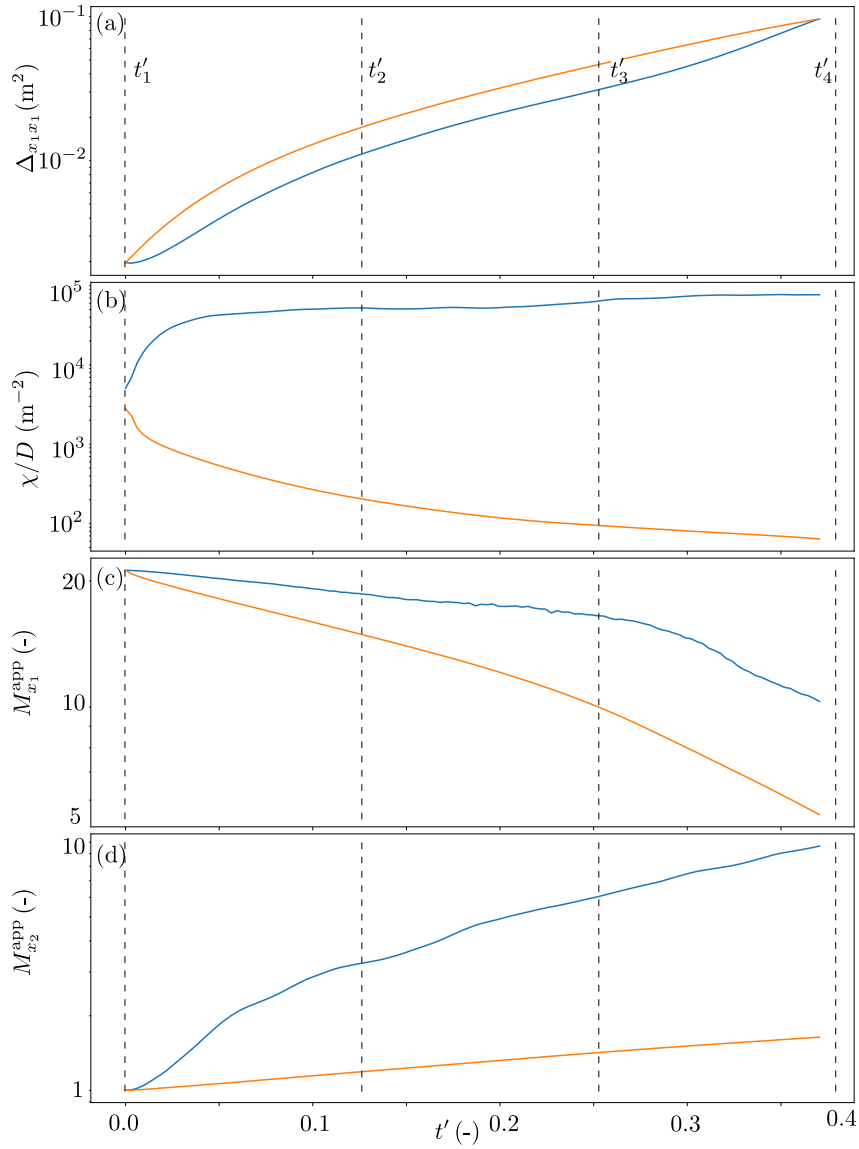

Figure 6. (a) Spreading of the solute, quantified by $\Delta_{x_1x_1}$, (b) mixing of the solute, quantified by χ/D and observed apparent mixing factors in the (c) x_1-direction, $M^{\mathrm{app}}_{x_1}$, and (d) x_2-direction, $M^{\mathrm{app}}_{x_2}$, for a solute pulse transported at (blue) high and (orange) low Péclet numbers. The plots are given in terms of t', the time normalized by the characteristic advective transport time-scale τ_{ADV}. The black vertical dashed lines, labeled as t'_1, t'_2, t'_3 and t'_4 mark the dimensionless times corresponding to the snapshots of the saline concentration field shown in Figure 5.

faster than the rate at which diffusion erases such gradients. The contrary occurs for the low Péclet case, where homogenization overcomes segregation.

The time-series of $M^{\mathrm{app}}_{x_1}$ (Figure 6c) decay from an initial value of ~20, to values of ~9 and ~5 at $t/t_{\mathrm{ADV}} \sim 0.4$, for the fast and slow tracer tests, respectively. As the tracer spreads along the x_1-direction, the domain becomes better connected along this direction, which explains the decay of $M^{\mathrm{app}}_{x_1}$ with time. This effect is more pronounced for the slow tracer test since diffusion is more efficient in spreading tracer mass along x_1. The time-series of $M^{\mathrm{app}}_{x_2}$ start at a value of 1, since $c(\mathbf{x})$ is then layered and the electrical conductivity is averaged arithmetically. For the fast tracer test, $M^{\mathrm{app}}_{x_2}$ increases by more than one order of magnitude by the end of the test, since the solute plume becomes more tortuous. For the slow test, $M^{\mathrm{app}}_{x_2}$ reaches a much smaller peak value.

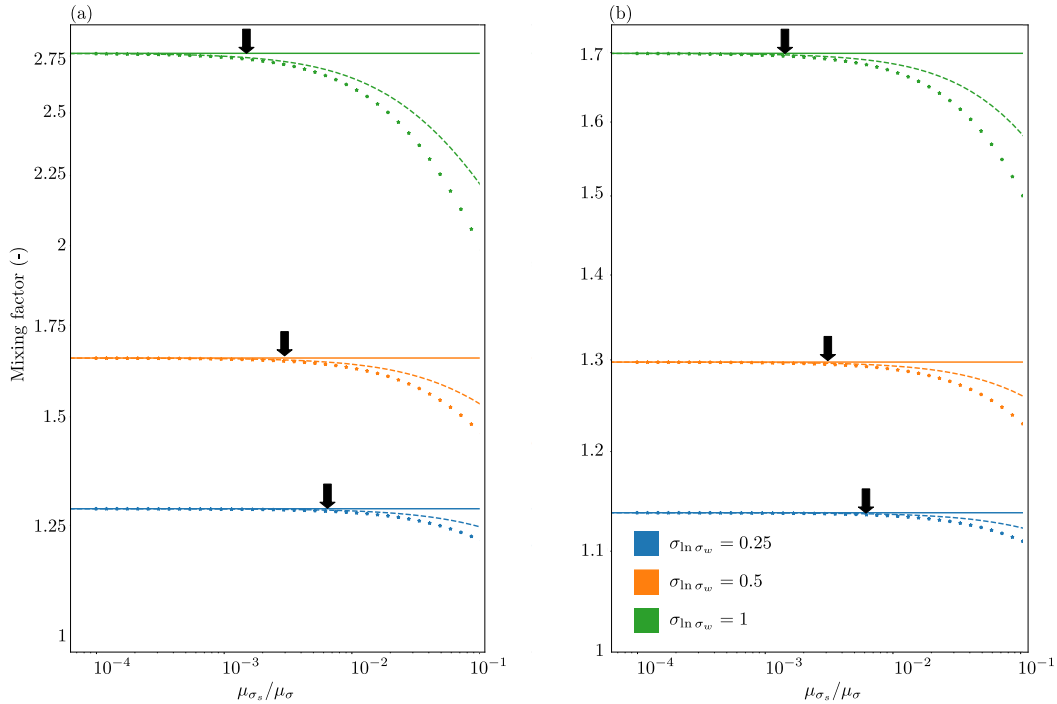

Figure 7. Comparison of M in the presence of surface conductivity for log-normally distributed ¡$\sigma_w(\mathbf{x})$-fields of fixed mean $\mu_{\sigma_w} = 1\ \mathrm{Sm}^{-1}$ and log-variances $\sigma^2_{\ln\sigma_w}$ of (blue) 0.25, (orange) 0.5 and (green) 1. The fields have (a) layered and (b) isotropic structures and the mixing factors are computed along the x_2-direction. (solid lines) the theoretical M (i.e., in the absence of surface conductivity) as reference, (solid stars) the apparent one M^{app}, in the presence of surface conductivity and (dashed line) the corrected one M^{corr}, using Equation 30 based on the high-salinity asymptotic limit. The black vertical arrows indicate the value described in the main text below which the correction is expected to be valid. The formation factor is $F = 10$.

4.3. Determination of M in the Presence of Surface Conductivity

We consider now apparent mixing factors M^{app} (Equation 26) measured in the presence of surface conductivity μ_{σ_s}. We compare M^{app} against the theoretical mixing factor M, defined in the absence of surface conductivity (see Section 3.2), and against the corrected mixing factor M^{corr}, obtained by applying Equation 30 that is valid in the high-salinity asymptotic limit.

4.3.1. Static Setting

We consider first layered and isotropic $\sigma_w(\mathbf{x})$-fields following a log-normal distribution of fixed mean value $\mu_{\sigma_w} = 1\ \mathrm{Sm}^{-1}$ and three different log-variances of $\sigma^2_{\ln\sigma_w} = 0.25$, 0.5 and 1. Each of the six test cases is evaluated for a range of values of μ_{σ_s} such that $\mu_{\sigma_s}/\mu_\sigma \in [0, 0.1]$, with $\mu_\sigma = \mu_{\sigma_w}/F$ and $F = 10$. To assess the departure from the high-salinity limit for these cases of heterogeneous $\sigma_w(\mathbf{x})$, we consider for each test case a reference minimum value of surface conductivity, given as 10% of a threshold value chosen to be $\exp\left[\mu_{\ln\sigma_w} - 3\sqrt{\sigma^2_{\ln\sigma_w}}\right]/F$, that is, three standard deviations away from the mean value of the underlying normal distribution.

For all cases, the ratio M^{app}/M is close to 1 for the reference value delimitating the high-salinity limit (black vertical arrows), indicating small errors when correcting within this limit. The apparent mixing factor M^{app} underestimates M as the ratio $\mu_{\sigma_s}/\mu_\sigma$ increases and the correction M^{corr} partially mitigates this effect (Figure 7). For instance, for the layered case (Figure 7a) with $\sigma^2_{\ln\sigma_w} = 0.25$, the ratio M^{app}/M is equal to 0.86 for the maximum considered value of surface conductivity $\mu_{\sigma_s}/\mu_\sigma = 0.1$, while the ratio M^{corr}/M yields 0.92. For $\sigma^2_{\ln\sigma_w} = 1$, M^{app}/M gives 0.52 for $\mu_{\sigma_s}/\mu_\sigma = 0.1$, whereas M^{corr}/M gives 0.64. For the isotropic case (Figure 7b), the errors are smaller. For instance, for $\sigma^2_{\ln\sigma_w} = 0.25$, the ratio M^{app}/M yields 0.94 for $\mu_{\sigma_s}/\mu_\sigma = 0.1$, whereas M^{corr}/M gives 0.97. For $\sigma^2_{\ln\sigma_w} = 1$, M^{app}/M and M^{corr}/M give 0.70 and 0.81, respectively.

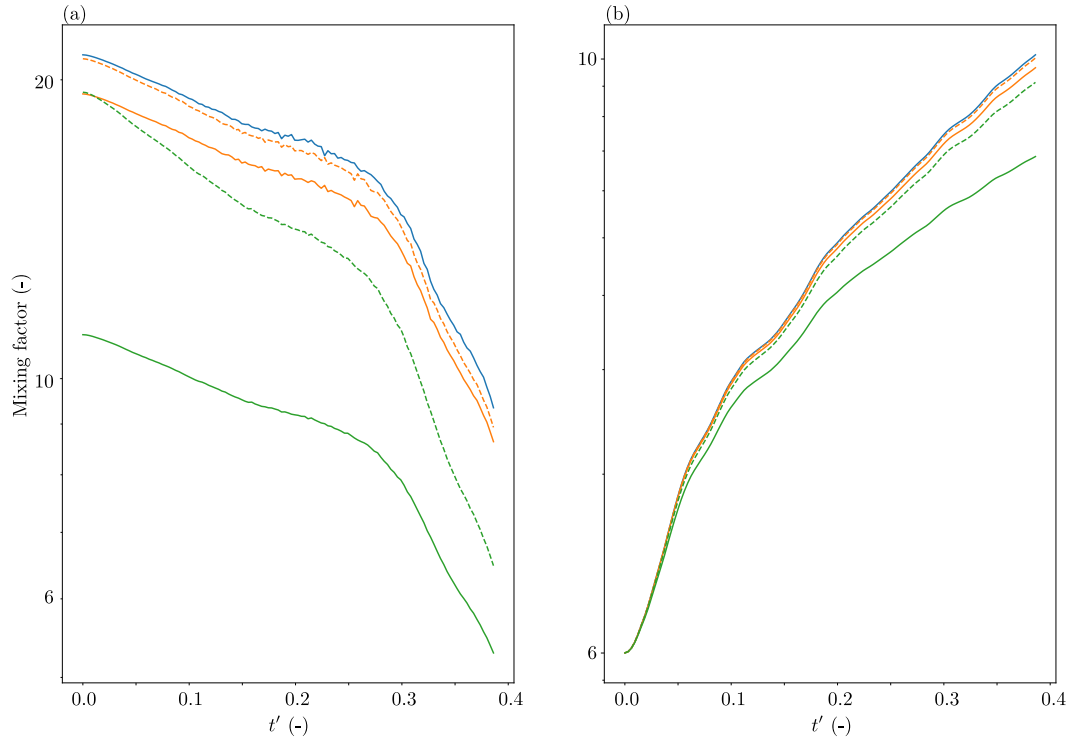

Figure 8. (a) (solid blue) Apparent mixing factor (Equation 26) in the x_1-direction as a function of dimensionless time t' for the tracer test in Figure 5a and apparent mixing factors in presence of surface conductivities μ_{σ_s} equal to (solid orange) $\mu_{\sigma_s} = 0.0001\ \mathrm{Sm}^{-1}$ and (solid green) $\mu_{\sigma_s} = 0.001\ \mathrm{Sm}^{-1}$ which represent, respectively, 10% and 100% of the background fluid conductivity divided by the formation factor. The corrected mixing factor M^{corr} (Equation 30) is also represented for the case of (dashed orange) $\mu_{\sigma_s} = 0.0001\ \mathrm{Sm}^{-1}$ for which the correction is supposed to be approximately valid and (dashed green) $\mu_{\sigma_s} = 0.001\ \mathrm{Sm}^{-1}$ for which the correction is invalid. (b) Apparent mixing factors in the x_2-direction with the same color coding. The formation factor is $F = 10$.

4.3.2. Dynamic Setting

We reconsider the tracer test at high Péclet number presented in Section 4.2.3, along with the corresponding apparent mixing factors measured in the absence of surface conductivity along the x_1 and x_2-directions, $M^{\mathrm{app}}_{x_1}$ (blue solid line, Figure 8a) and $M^{\mathrm{app}}_{x_2}$ (blue solid line, Figure 8b), respectively. We simulate apparent mixing factors $M^{\mathrm{app,S}}_{x_1}$ and $M^{\mathrm{app,S}}_{x_2}$, by adding surface conductivities of $\mu_{\sigma_s} = 0.0001\ \mathrm{Sm}^{-1}$ and $\mu_{\sigma_s} = 0.001\ \mathrm{Sm}^{-1}$ to the underlying time-evolving fluid conductivity field (Figure 5a), values which represent 10% and 100% of the background conductivity (i.e., fluid conductivity divided by formation factor) and are considered to lie in the vicinity and well outside the high-salinity asymptotic limit, respectively.

For the x_1-direction (Figure 8a) and $\mu_{\sigma_s} = 0.0001\ \mathrm{Sm}^{-1}$, the ratio between the measured apparent mixing factor $M^{\mathrm{app,S}}_{x_1}$ (orange solid line) and $M^{\mathrm{app}}_{x_1}$, averaged over the observation time window, is $M^{\mathrm{app,S}}_{x_1}/M^{\mathrm{app}}_{x_1} \sim 0.91$, whereas the corresponding ratio for the corrected mixing factor $M^{\mathrm{corr}}_{x_1}$ (orange dashed line) gives $M^{\mathrm{corr}}_{x_1}/M^{\mathrm{app}}_{x_1} \sim 0.98$. The measured $M^{\mathrm{app,S}}_{x_1}$ for the case $\mu_{\sigma_s} = 0.001\ \mathrm{Sm}^{-1}$ (green solid line), leads to $M^{\mathrm{app,S}}_{x_1}/M^{\mathrm{app}}_{x_1} \sim 0.53$ and the corrected mixing factor M^{corr} (green dashed line) yields $M^{\mathrm{corr}}_{x_1}/M^{\mathrm{app}}_{x_1} \sim 0.81$. For the x_2-direction the behavior is similar.

5. Discussion

5.1. Assumptions Underlying the Definition of the Mixing Factor M

The formal definition of the mixing factor M (Equation 21) assumes (a) an ergodic fluid conductivity field $\sigma_w(\mathbf{x})$, (b) zero surface conductivity μ_{σ_s} and (c) a spatially constant formation factor $F(\mathbf{x})$. In addition, we provide operational (Equation 26) and formal (Equation 29) definitions to measure and model, respectively, an apparent

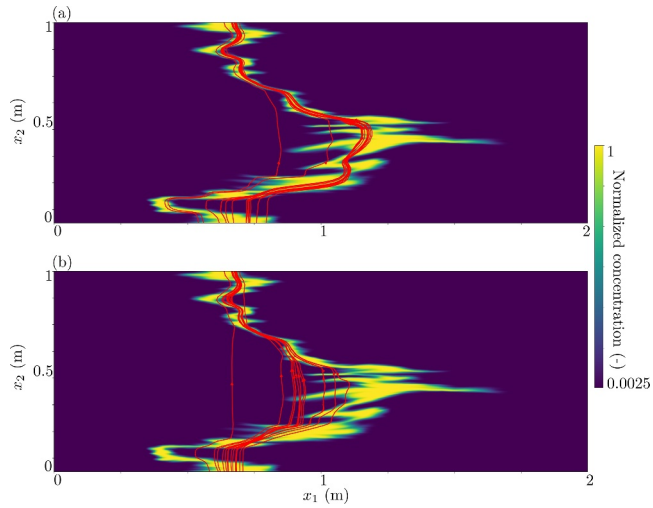

Figure 9. Electrical current streamlines generated by imposing an electrical potential difference along the x_2-direction for conductivity fields with surface conductivity μ_{σ_s} equal to (a) 0 S m^{-1} and (b) 0.001 S m^{-1}, which represents 100% of the background conductivity. The ratio between tracer and background fluid conductivities is 400. The background images represent the saline concentration field normalized by its maximum value.

mixing factor M^{app} under general conditions. Below, we discuss critically the assumptions underlying the formal definition of M.

5.1.1. Ergodicity of the Fluid Conductivity Field

Ergodicity (e.g., Christakos, 2012; Rubin, 2003) implies that the scale of observation of σ_{eq} is large compared to the typical size of the structures in $\sigma_w(\mathbf{x})$. This assumption allows neglecting the net flux of fluctuating energy over the boundaries of the domain (Equation A7), subsequently leading to Equation 21. In many practical applications, $\sigma_w(\mathbf{x})$ is non-stationary or non-ergodic, for instance, as shown in Figures 4a–4e.

For the non-ergodic case, the apparent mixing factor M^{app} depends on M as:

$$\frac{1}{M^{\text{app}}} = \frac{2}{M} - 1 + \frac{1}{V}\int e'^2 dV, \tag{32}$$

which is obtained by combining Equations 21 and 29 under the assumption of a constant formation factor and no surface conductivity. The difference between M^{app} and M could be used as an electrical measure of departure from ergodicity for $\sigma_w(\mathbf{x})$ and, consequently, for the salinity $c(\mathbf{x})$.

5.1.2. High-Salinity Limit

In presence of surface conductivity, the proposed correction of M^{app} into M (Equation 30) performs well provided that the conductivity field $\sigma(\mathbf{x})$ locally satisfies the high-salinity asymptotic limit, that is, the ratio between the first and second terms of the RHS of Equation 19 is large for all $\mathbf{x}$. In practice, the surface conductivity μ_{σ_s} could be estimated from induced polarization measurements (e.g., Binley & Slater, 2020; Slater & Lesmes, 2002). The presence of μ_{σ_s} is equivalent to placing an electrical conductor that acts in parallel to $\sigma_w(\mathbf{x})$. When no surface conductivity is present, the electrical streamlines follow the tracer body more closely (Figure 9a), as compared to the case with surface conductivity (Figure 9b), for which shorter current paths appear. The net effect is that the equivalent electrical conductivity σ_{eq} is less sensitive to heterogeneity in $\sigma_w(\mathbf{x})$ or, equivalently, the apparent mixing factor M^{app} (Equation 26) becomes smaller than the theoretical value M, as shown in Section 4.3.

5.1.3. Constant Formation Factor F

The mixing factor M captures electrical signatures arising from heterogeneity in $\sigma_w(\mathbf{x})$, within a sample assumed to have a spatially constant formation factor $F(\mathbf{x})$. The patterns of spatial heterogeneity in the fields $\sigma_w(\mathbf{x})$ presented in Figures 1, 2, 5, and 9 result from solute transport in domains with heterogeneous permeability $k(\mathbf{x})$. Indeed, heterogeneity in $\sigma_w(\mathbf{x})$ is typically triggered by heterogeneity in the permeability field $k(\mathbf{x})$, for some given viscosity of the fluid and tracer injection pattern. The link between $k(\mathbf{x})$ and F has been studied in great detail, for instance based on mercury injection experiments (Katz & Thompson, 1986). Furthermore, the following relationship has been proposed Avellaneda and Torquato (1991):

$$k(\mathbf{x}) = \frac{l^2}{8F(\mathbf{x})}, \tag{33}$$

where l is a length parameter characterizing the porous medium in terms of the viscous relaxation times associated to the harmonic solution of the Navier-Stokes equation (e.g., Avellaneda & Torquato, 1991).

Consequently, it might seem paradoxical to consider heterogeneity in $\sigma_w(\mathbf{x})$, while simultaneously setting a homogeneous $F(\mathbf{x})$-field. However, heterogeneity in $k(\mathbf{x})$ is in general of much larger amplitude than heterogeneity in $F(\mathbf{x})$ and there is often no significant general correlation between the two (e.g., Purvance & Andricevic, 2000). This, combined with Equation 33, suggests that the strongest influence in $k(\mathbf{x})$-heterogeneity emerges as a result of spatial variations in the characteristic length l rather than $F(\mathbf{x})$, given the quadratic

dependence of the former. In addition, one should note that most time-lapse ERT interpretations assume constant $F(\mathbf{x})$ over the entire domain and, similarly, most tracer inversions aimed at inferring heterogeneous distributions of hydraulic conductivity assume porosity to be constant. Thus, assuming constant $F(\mathbf{x})$ within the model domain or measurement scale of the electrical data appears to be a reasonable first-order approximation for most cases. Note that the impact of a spatially variable $F(\mathbf{x})$ can be studied using Equation 29. For instance, one could evaluate Equation 29 for $\sigma_w(\mathbf{x})$ and $F(\mathbf{x})$ consisting of binary distributions that represent the mobile and immobile domains of dual-domain media (e.g., Haggerty & Gorelick, 1995). From here, one could establish links with bi-continuum models (e.g., Day-Lewis et al., 2017; Singha et al., 2007) of equivalent electrical conductivity.

5.2. Using the Mixing Factor M in Hydrogeophysical Studies

An open question for future research is how to best incorporate the mixing factor M, and the generalization of the high-salinity limit (Equation 20), in field-based hydrogeophysical studies. The parameter M could be applied either at the spatially variable resolution scale of geophysical tomograms or at the discretization scales of hydrogeological or geophysical forward models. In the former case, M could serve at an interpretation stage as a fitting parameter, chosen such that the inferred saline mass in the system is in accordance with prior knowledge (e.g., the amount of injected salt). It would then quantify unaccounted solute heterogeneity due to the smoothing introduced by inverse model regularization, the latter applied in classical deterministic ERT approaches to yield unique results (e.g., Constable et al., 1987). For instance, if the classical petrophysical relationship of Equation 15 leads to an apparent mass recovery of 10% (e.g., Camporese et al., 2011; Singha & Gorelick, 2005), this implies that the inferred M would be 10, if assumed to be spatially constant across the model. If M would be applied at the discretization scales of hydrogeological or geophysical forward models, one could imagine a standard groundwater model based on the advection-dispersion equation in which small-scale heterogeneity is not represented because of computational costs or inadequate knowledge. Equation 20 could then be used to translate the simulated locally homogeneous salinity into an effective electrical conductivity within a coupled hydrogeophysical framework (e.g., Hinnell et al., 2010; Kowalsky et al., 2005). Such information could then guide interpretations, using the presented results and relationships (e.g., Sections 4.2.2 and 4.2.3), and answer questions such as: what is the degree of saline heterogeneity within the length scales that are unresolved by the inversion or by the forward model? It is clear that including M as a parameter in the inversion implies an additional degree of freedom (or more if assumed spatially variable), possibly leading to non-uniqueness issues in deterministic inversion problems, unless strong prior constraints are available that can be incorporated in the modeling. Despite this, including M still enhances the modeling task, as it enables investigating trade-offs between resolving large-scale or small-scale heterogeneity. Several of our examples demonstrate that M and M^{app} are very different in the direction parallel and perpendicular to flow. This renders the electrical conductivity anisotropic. With an appropriate electrical modeling solver, it would be possible to incorporate such effects in the electrical forward modeling. Probabilistic inversion approaches (e.g., Laloy et al., 2012; Linde & Vrugt, 2013; Tarantola, 2005) could also be explored to estimate the joint posterior probability density function of the target parameters μ_{σ_w} and M, conditioned to the ERT data. Alternatively, the effect of such small-scale heterogeneity could be integrated out to avoid biased results (e.g., Friedli et al., 2022, 2023). Finally, it will be important to consider if there is non-negligible surface conductivity μ_{σ_s} or heterogeneous formation factor F to be accounted, and corrected for (Equation 30). Future work needs to explore these ideas and demonstrations on field data are important future venues for research.

6. Conclusions

Electrical and electromagnetic geophysical methods can provide valuable information about the state and transport of solutes with applications to groundwater prospection, pollution and tracer monitoring, or inference of hydraulic conductivity by hydrogeophysical inversions. Almost all such studies have ignored saline heterogeneity below the averaging volume inherent to measurements, forward modeling or inversions, leading sometimes to biased and unphysical results such as apparent mass loss when interpreting tracer experiments. One reason for the current practice is the lack of a suitable interpretative framework that accounts for such unresolved small-scale variability. We have generalized the high-salinity asymptotic limit of electrical conduction at the continuous (e.g., Darcy) scale, by introducing a new petrophysical parameter, the mixing factor M, which accounts for the effect of saline heterogeneity on the equivalent electrical conductivity tensor. We provide an explicit link between M and fluid electrical conductivity heterogeneity, via a closed-form

expression in terms of the volume average of the product between the mean-removed electric and fluid electrical conductivity fields, respectively, $e'(\mathbf{x})$ and $\sigma'_w(\mathbf{x})$, by assuming ergodicity in $\sigma_w(\mathbf{x})$, zero surface conductivity μ_{σ_s} and homogeneous formation factor F. In addition, we provide operational and formal definitions for an apparent mixing factor M^{app}, which is valid under more general conditions. Considering 2-D examples of log-normal $\sigma_w(\mathbf{x})$-fields, we demonstrate how the M-tensor maps univocally to the variance and anisotropy of $\sigma_w(\mathbf{x})$. Also, when we let $\sigma_w(\mathbf{x})$ homogenize by diffusion, the time-series of M are sensitive to the characteristic temporal scale of diffusion and allow constraining the mixing evolution of the field. The sensitivity of M to the connectivity and anisotropy of the spatial patterns in $\sigma_w(\mathbf{x})$ makes M also sensitive to the predominant directions along which concentration gradients exist. Under diffusive and advective transport, the time-series of M help distinguishing the Péclet number. Our petrophysical relationship allows separating the electrical effects associated to the mean value and to heterogeneity of the underlying fluid conductivity field. Future work needs to address how to incorporate such relationship into existing forward and inverse hydrogeophysical modeling workflows. It is further important to gain understanding on the relationship between $e'(\mathbf{x})$ and $\sigma'_w(\mathbf{x})$ beyond the ergodic log-normal case and to develop upscaling relationships that enable to link M with non-ergodic $\sigma_w(\mathbf{x})$-fields. It is also necessary to study the electrical signatures captured by M^{app} due to heterogeneity in F and μ_{σ_s}-values beyond the high-salinity limit considered in the present work. Interpretation workflows or inversion methodologies integrating the concept of the mixing factor in field-scale studies remain to be developed.

Appendix A: Derivation of the Mixing Factor M

We derive here our generalization of the high-salinity asymptotic limit of electrical conduction in presence of a heterogeneous salinity field, that is, Equation 20, along with the definition of the mixing factor M, Equation 21. The obtained expressions are based on the energy representation of equivalent electrical conductivity and are similar to the problem formulation presented by (e.g., Dagan, 1993). We express the conductivity field $\sigma(\mathbf{x})$ as $\sigma(\mathbf{x}) = \sigma_w(\mathbf{x})/F + \mu_{\sigma_s}$, that is, using the petrophysical expression of the form of Equation 17, that is valid in the high-salinity asymptotic limit, but letting the fluid conductivity term to be variable. This implies assuming that the ratio $\sigma_w(\mathbf{x})/\mu_{\sigma_s}$ is very large for all $\mathbf{x}$. We decompose the normalized electric- and fluid conductivity fields, $\mathbf{e}(\mathbf{x})$ and $\sigma_w(\mathbf{x})$, into their mean and fluctuating parts as $\mathbf{e}(\mathbf{x}) = 1 + \mathbf{e}'(\mathbf{x})$ and $\sigma(\mathbf{x}) = \left(\mu_{\sigma_w} + \sigma'_w(\mathbf{x})\right)/F + \mu_{\sigma_s}$. Substituting this into Equation 13, separating terms involving spatially constant and spatially varying terms and, expanding the dot products, yields:

$$\sigma_{\text{eq}} = \frac{1}{V}\int_V \left[\left(\frac{\mu_{\sigma_w}}{F} + \mu_{\sigma_s}\right)(1 + 2e'_{x_1} + \mathbf{e}'\cdot\mathbf{e}')\frac{\sigma'_w}{F} + 2\frac{\sigma'_w}{F}e'_{x_1} + \frac{\sigma'_w}{F}\mathbf{e}'\cdot\mathbf{e}'\right] dV. \tag{A1}$$

Both $\mathbf{e}'(\mathbf{x})$ and $\sigma'(\mathbf{x})$ have zero mean by construction and, consequently, terms containing their products with constant quantities, integrated over V, vanish exactly. Thus, Equation A1 reduces to:

$$\sigma_{\text{eq}} = \frac{1}{V}\int_V \left[\left(\frac{\mu_{\sigma_w}}{F} + \mu_{\sigma_s}\right) + \left(\frac{\mu_{\sigma_w}}{F} + \mu_{\sigma_s}\right)\mathbf{e}'\cdot\mathbf{e}' + 2\frac{\sigma'_w}{F}e'_{x_1} + \frac{\sigma'_w}{F}\mathbf{e}'\cdot\mathbf{e}'\right] dV. \tag{A2}$$

The last three terms of the right-hand side (RHS) of Equation A2 are related to each other. To see this, we first express the current density $\mathbf{J}(\mathbf{x})$ as the sum of its mean and fluctuating parts, respectively, $\mathbf{J}_0$ and $\mathbf{J}'(\mathbf{x})$, and apply Ohm's law, normalized by the modulus of the imposed field, E_0. We write

$$\left[\frac{\mu_{\sigma_w} + \sigma'_w}{F} + \mu_{\sigma_s}\right][\hat{x}_1 + \mathbf{e}'] = \frac{1}{E_0}(\mathbf{J}_0 + \mathbf{J}'). \tag{A3}$$

Multiplying Equation A3 by $\mathbf{e}'(\mathbf{x})$, integrating over V and distributing products, we obtain:

$$\int_V \left(\frac{\mu_{\sigma_w}}{F} + \mu_{\sigma_s}\right)e'_{x_1} + \frac{\sigma'_w}{F}e'_{x_1} + \left(\frac{\mu_{\sigma_w}}{F} + \mu_{\sigma_s}\right)\mathbf{e}'\cdot\mathbf{e}' + \frac{\sigma'_w}{F}\mathbf{e}'\mathbf{e}'dV = \frac{1}{E_0}\int_V \mathbf{e}'\cdot\mathbf{J}_0 + \mathbf{e}'\cdot\mathbf{J}'dV. \tag{A4}$$

Equation A4 expresses an identity for the dissipated power in the sample due to the secondary field $\mathbf{e}'(\mathbf{x})$. The first terms of the LHS and the RHS of Equation A4 vanish because these involve integration of products of a constant and a zero-mean fluctuating quantity. Assuming that $\sigma_w(\mathbf{x})$ is ergodic (e.g., Christakos, 2012; Rubin, 2003), then the remaining term of the RHS vanishes because $\mathbf{e}'$ and $\mathbf{J}'$ are orthogonal to each other in the average, or, equivalently (e.g., Torquato & Haslach, 2002), because:

$$\lim_{V\to\infty}\frac{1}{V}\int_S U'\mathbf{J}'\cdot\hat{\mathbf{n}}dS' = 0, \tag{A5}$$

where $U'(\mathbf{x})$ is the fluctuating electrical potential and S is the bounding surface of the volume. The remaining terms of Equation A4 do not vanish in general. This yields:

$$\int_V\left(\frac{\mu_{\sigma_w}}{F}+\mu_{\sigma_s}\right)\mathbf{e}'\cdot\mathbf{e}'dV+\int_V\frac{\sigma_w'}{F}e_{x_1}'+\frac{\sigma_w'}{F}\mathbf{e}'\cdot\mathbf{e}'dV=0. \tag{A6}$$

We use the identity of Equation A6 to replace the second and fourth terms of the RHS of Equation A2 and arrive at

$$\sigma_{\text{eq}}=\frac{1}{V}\int_V\left(\frac{\mu_{\sigma_w}+\mu_{\sigma_s}}{F}\right)dV+\frac{1}{V}\int_V\frac{\sigma_w'}{F}e_{x_1}'dV. \tag{A7}$$

Distributing the products in Equation A7, replacing μ_{σ_s} by its expression in the high-salinity asymptotic limit, that is, $\mu_{\sigma_s}=2\mu_{\Sigma_s}/F\Lambda$ and, factorizing μ_{σ_w}/F, we finally arrive at:

$$\sigma_{\text{eq}}=\frac{\mu_{\sigma_w}}{F}\left(1+\frac{1}{\mu_{\sigma_w}V}\int_V\sigma_w'e_{x_1}'dV+\frac{2}{\Lambda}\frac{\mu_{\Sigma_s}}{\mu_{\sigma_w}}\right), \tag{A8}$$

or,

$$\sigma_{\text{eq}}=\frac{\mu_{\sigma_w}}{F}\left(\frac{1}{M}+\frac{2}{\Lambda}\frac{\mu_{\Sigma_s}}{\mu_{\sigma_w}}\right), \tag{A9}$$

which is a generalized form of the expression by Johnson et al. (1986), accounting for fluid conductivity heterogeneity, with the mixing factor M being defined, for an imposed current in the x_1-direction and in the absence of surface conductivity, as:

$$\frac{1}{M}=1+\frac{1}{\mu_{\sigma_w}V}\int_V\sigma_w'e_{x_1}'dV. \tag{A10}$$

Appendix B: Relationship Between Fluid Conductivity and Electric Field Fluctuations

We illustrate examples of the relationship between fluid conductivity and electric field fluctuations, respectively, $\sigma_w'(\mathbf{x})$ and $e'(\mathbf{x})$, that influences the mixing factor M (Equation 21). We consider well-known cases of 2-D heterogeneity for $\sigma_w(\mathbf{x})$, namely, log-normal $\sigma_w(\mathbf{x})$-fields with exponential covariance function, fixed mean value of $\mu_{\sigma_w}=1\,\text{Sm}^{-1}$ and varying variance. We focus on fields having layered and isotropic structures with anisotropy factor $\lambda=\infty$ and $\lambda=1$, with $\lambda:=I_{x_1}/I_{x_2}$, the ratio of the integral scales along the x_1- and x_2-directions (e.g., Rubin, 2003). The integral scale I_{x_2} is set to 0.02 m. We solve numerically Equation 11 on domains of 1 m side length with constant porosity and formation factors of 0.2 and 10, respectively, with imposed boundary conditions of a unit voltage drop along x_1 or x_2 and zero current flux along the top and bottom or right and left boundaries, respectively.

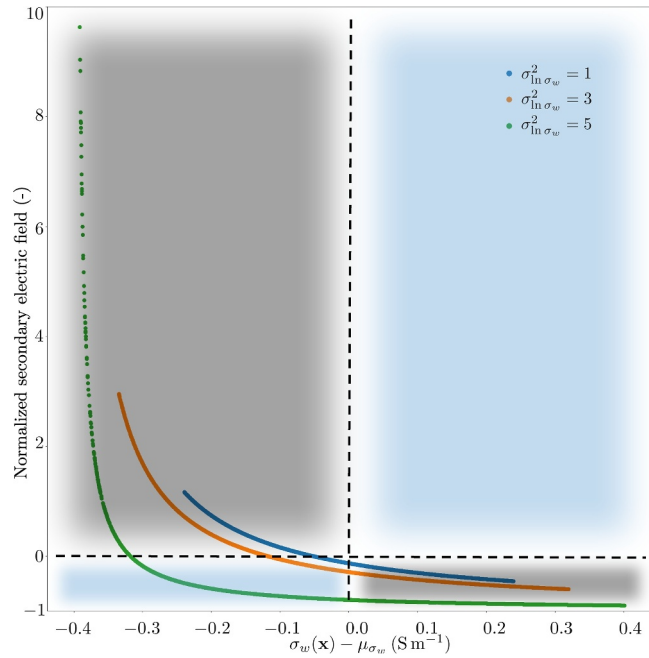

Figure B1. Scatter plot of fluid electrical conductivity field fluctuations $\sigma'_w(\mathbf{x})$ $\left(=\sigma_w(\mathbf{x}) - \mu_{\sigma_w(\mathbf{x})}\right)$ versus normalized secondary electric field $e'_{x_2}(\mathbf{x})$ as a function of the variance of $\sigma_w(\mathbf{x})$. Here, $\sigma_w(\mathbf{x})$ has a layered configuration and the electrical field is imposed perpendicularly to the layering. The first and third (second and fourth) quadrants of the Cartesian axes are indicated with light blue (gray-colored) shadows. For the first and third quadrants, the product of $e'_{x_2}(\mathbf{x})$ and $\sigma'_w(\mathbf{x})$ is positive, whereas for the other two, it is negative and their sum is larger than the sum of the other contributions, leading to a decrease in the equivalent electrical conductivity compared with the case of a constant salinity.

B1. Layered Case

We plot $\sigma'_w(\mathbf{x})$ $\left(=\sigma_w(\mathbf{x}) - \mu_{\sigma_w}\right)$ against $e'_{x_2}(\mathbf{x})$ for three different layered log-normal $\sigma_w(\mathbf{x})$-fields having different variances (Figure B1). For the smaller variance $\sigma^2_{\sigma_w} = 0.01\,\mathrm{S^2 m^{-2}}$ (Figure B1, blue dots), $\sigma'_w(\mathbf{x})$ takes values within $[-0.25, 0.25]$ S m^{-1}, which are univocally mapped (i.e., along a line) to values in $e'_{x_2}(\mathbf{x})$ that range within $[-0.4, 1]$. As the variance increases (Figure B1, orange and green dots), so does the range for the values taken by $\sigma'_w(\mathbf{x})$ and $e'_{x_2}(\mathbf{x})$. Also, the asymptote $e'_{x_2}(\mathbf{x}) = -1$ is increasingly approached, the former corresponding to the case where there is an isolating layer and the modulus of the secondary electric field equates the modulus of the imposed primary electric field, leading to zero current flow. Note that any given dot in Figure B1 represents one energy contribution to the integral in Equation 21. One simply has to multiply a given value of the horizontal axis in Figure B1 by the associated value on the vertical axis to obtain the corresponding contribution. Positive (negative) contributions come from the first and third (second and fourth) quadrants, which are indicated in Figure B1 with light blue (gray-colored) shadows. As the variance of $\sigma'_w(\mathbf{x})$ increases, there are more negative contributions to the integral in the RHS of Equation 21 (i.e., more weight of the $\sigma'_w(\mathbf{x})$-$e'_{x_2}(\mathbf{x})$ curve in the second and fourth quadrants), leading to a lower value of $\sigma^{x_2}_{\mathrm{eq}}$ than σ_{A}. For all the considered layered cases, the energy contributions fall on well-defined lines without any scatter; this is a consequence of the electrical current paths being pre-determined by the imposed layered structure.

B2. Isotropic Case

As for the layered case, we plot $\sigma'_w(\mathbf{x})$ $\left(=\sigma_w(\mathbf{x}) - \mu_{\sigma_w}\right)$ against $e'_{x_1}(\mathbf{x})$ for three log-normal isotropic $\sigma_w(\mathbf{x})$-fields having different variances (Figure B2). The integral scale is set to 0.02 m. For a variance of the log-field $\sigma^2_{\ln\sigma_w} = 1$ (Figure B2, blue dots), $\sigma'_w(\mathbf{x})$ takes values within $[-0.1, 6]$ that are mapped to values in $e'_{x_1}(\mathbf{x})$ ranging within $[-1, 8]$. The horizontal asymptote $e'_{x_1}(\mathbf{x}) = -1$ is far from being reached. In contrast to the layered case, the $\sigma'_w(\mathbf{x})$-$e'_{x_1}(\mathbf{x})$ relationship is non-unique, that is, a given value for $\sigma'_w(\mathbf{x})$ maps into different values for $e'_{x_1}(\mathbf{x})$. With

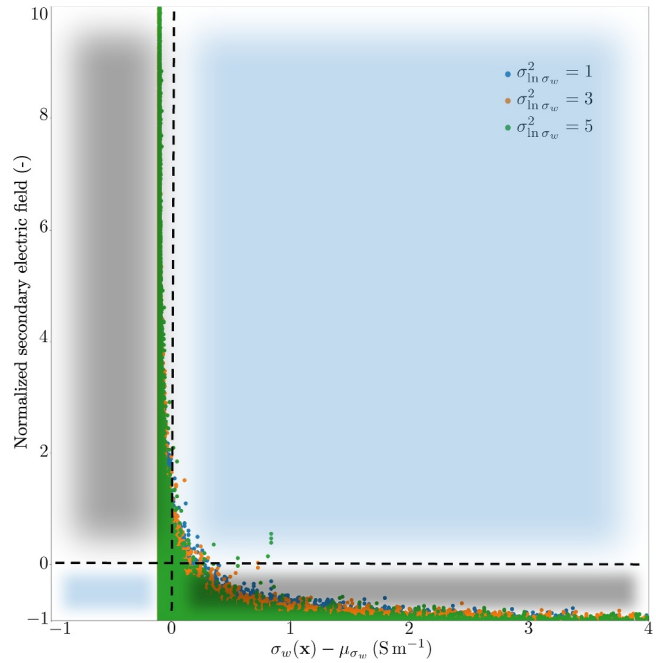

Figure B2. Scatter plot of fluid electrical conductivity field fluctuations $\sigma'_w(\mathbf{x})$ $\left(=\sigma_w(\mathbf{x}) - \mu_{\sigma(\mathbf{x})}\right)$ versus the secondary electric field $e'(\mathbf{x})$, as a function of the log-variance of $\sigma_w(\mathbf{x})$. Here, $\sigma_w(\mathbf{x})$ is a log-normal isotropic field. The first and third (second and fourth) quadrants of the Cartesian axes are indicated with the light blue (gray-colored) shadows. For the first and third quadrants, the product of $e'(\mathbf{x})$ and $\sigma'_w(\mathbf{x})$ is positive, whereas for the other two it is negative. The negative terms dominate increasingly with a higher variance, leading to increasing values of the mixing factor.

the additional degree of freedom offered by the 2-D heterogeneity, the electrical current pathways will organize to minimize the energy dissipation, thereby, making the relationship dependent on neighboring features.

Data Availability Statement

The data presented in this manuscript can be found in the Zenodo repository (Visentini, 2024) under https://doi.org/10.5281/zenodo.11068781. The data were generated using publicly available software packages. For simulating electrical potential distributions we used the Python package pyGIMLi (Rücker et al., 2017). Flow and transport simulations were run using Floppy (Bakker et al., 2016), MODFLOW-2005 (Harbaugh, 2005) and MT3D-USGS (Bedekar et al., 2016).

Acknowledgments
Open Access funding provided by University of Lausanne. This work has received funding from the Swiss National Science Foundation under Grant 200020-184574. We are grateful for the insightful comments provided by Associate Editor Lee Slater, Olaf Cirpka and one anonymous reviewer. We thank Editor Xavier Sánchez Vila for handling the review process.

References

Adrian, R., Christensen, K., & Liu, Z.-C. (2000). Analysis and interpretation of instantaneous turbulent velocity fields. *Experiments in Fluids*, *29*(3), 275–290. https://doi.org/10.1007/s003489900087

Archie, G. E. (1942). The electrical resistivity log as an aid in determining some reservoir characteristics. *Transactions of the American Institute of Mining, Metallurgical, and Petroleum Engineers*, *146*(01), 54–62. https://doi.org/10.2118/942054-G

Avellaneda, M., & Torquato, S. (1991). Rigorous link between fluid permeability, electrical conductivity, and relaxation times for transport in porous media. *Physics of Fluids A: Fluid Dynamics*, *3*(11), 2529–2540. https://doi.org/10.1063/1.858194

Bakker, M., Post, V., Langevin, C. D., Hughes, J. D., White, J., Starn, J., & Fienen, M. N. (2016). Scripting MODFLOW model development using Python and FloPy [Software]. *Ground Water*, *54*(5), 733–739. https://doi.org/10.1111/gwat.12413

Bear, J. (1972). *Dynamics of fluids in porous media*. Dover Publications.

Bedekar, V., Morway, E. D., Langevin, C. D., & Tonkin, M. J. (2016). MT3D-USGS version 1: A US Geological Survey release of MT3DMS updated with new and expanded transport capabilities for use with MODFLOW [Software] Tech. rep. *US Geological Survey*. https://doi.org/10.3133/tm6A53

Bender, C. M., & Orszag, S. A. (1999). In *Advanced mathematical methods for scientists and engineers I: Asymptotic methods and perturbation theory* (Vol. 1). Springer Science & Business Media.

Berkowitz, B., Cortis, A., Dentz, M., & Scher, H. (2006). Modeling non-Fickian transport in geological formations as a continuous time random walk. *Reviews of Geophysics*, *44*(RG2003). https://doi.org/10.1029/2005RG000178

Bernabé, Y., & Revil, A. (1995). Pore-scale heterogeneity, energy dissipation and the transport properties of rocks. *Geophysical Research Letters*, *22*(12), 1529–1532. https://doi.org/10.1029/95GL01418

Binley, A., Hubbard, S. S., Huisman, J. A., Revil, A., Robinson, D. A., Singha, K., & Slater, L. D. (2015). The emergence of hydrogeophysics for improved understanding of subsurface processes over multiple scales. *Water Resources Research*, *51*(6), 3837–3866. https://doi.org/10.1002/2015WR017016

Binley, A., & Slater, L. (2020). *Resistivity and induced polarization: Theory and applications to the near surface Earth*. Cambridge University Press. https://doi.org/10.1017/9781108685955

Bussian, A. (1983). Electrical conductance in a porous medium. *Geophysics*, *48*(9), 1258–1268. https://doi.org/10.1190/1.1441549

Camporese, M., Cassiani, G., Deiana, R., & Salandin, P. (2011). Assessment of local hydraulic properties from electrical resistivity tomography monitoring of a three-dimensional synthetic tracer test experiment. *Water Resources Research*, *47*(W12508). https://doi.org/10.1029/2011WR010528

Cassiani, G., Bruno, V., Villa, A., Fusi, N., & Binley, A. M. (2006). A saline trace test monitored via time-lapse surface electrical resistivity tomography. *Journal of Applied Geophysics*, *59*(3), 244–259. https://doi.org/10.1016/j.jappgeo.2005.10.007

Chelidze, T., & Gueguen, Y. (1999). Electrical spectroscopy of porous rocks: A review—I. Theoretical models. *Geophysical Journal International*, *137*(1), 1–15. https://doi.org/10.1046/j.1365-246x.1999.00799.x

Choy, T. C. (2015). In *Effective medium theory: Principles and applications* (Vol. 165). Oxford University Press.

Christakos, G. (2012). Random field models in Earth sciences. *Courier Corporation*.

Constable, S. C., Parker, R. L., & Constable, C. G. (1987). Occam's inversion: A practical algorithm for generating smooth models from electromagnetic sounding data. *Geophysics*, *52*(3), 289–300. https://doi.org/10.1190/1.1442303

Cortis, A., Gallo, C., Scher, H., & Berkowitz, B. (2004). Numerical simulation of non-Fickian transport in geological formations with multiple-scale heterogeneities. *Water Resources Research*, *40*(W04209). https://doi.org/10.1029/2003WR002750

Dagan, G. (1979). Models of groundwater flow in statistically homogeneous porous formations. *Water Resources Research*, *15*(1), 47–63. https://doi.org/10.1029/WR015i001p00047

Dagan, G. (1989). *Flow and transport in porous formations*. Springer-Verlag Berlin Heidelberg.

Dagan, G. (1993). Higher-order correction of effective permeability of heterogeneous isotropic formations of lognormal conductivity distribution. *Transport in Porous Media*, *12*(3), 279–290. https://doi.org/10.1007/BF00624462

Daigle, H. (2016). Application of critical path analysis for permeability prediction in natural porous media. *Advances in Water Resources*, *96*, 43–54. https://doi.org/10.1016/j.advwatres.2016.06.016

Day-Lewis, F. D., Linde, N., Haggerty, R., Singha, K., & Briggs, M. A. (2017). Pore network modeling of the electrical signature of solute transport in dual-domain media. *Geophysical Research Letters*, *44*(10), 4908–4916. https://doi.org/10.1002/2017GL073326

Day-Lewis, F. D., & Singha, K. (2008). Geoelectrical inference of mass transfer parameters using temporal moments. *Water Resources Research*, *44*(W05201). https://doi.org/10.1029/2007WR006750

Dentz, M., Le Borgne, T., Englert, A., & Bijeljic, B. (2011). Mixing, spreading and reaction in heterogeneous media: A brief review. *Journal of Contaminant Hydrology*, *120*, 1–17. https://doi.org/10.1016/j.jconhyd.2010.05.002

Dentz, M., Le Borgne, T., Lester, D. R., & de Barros, F. P. (2016). Mixing in groundwater. In *The handbook of groundwater engineering* (pp. 401–430). CRC Press.

Doetsch, J., Linde, N., Vogt, T., Binley, A., & Green, A. G. (2012). Imaging and quantifying salt-tracer transport in a riparian groundwater system by means of 3-D ERT monitoring. *Geophysics*, *77*(5), B207–B218. https://doi.org/10.1190/geo2012-0046.1

Dykaar, B. B., & Kitanidis, P. K. (1993). Transmissivity of a heterogeneous formation. *Water Resources Research*, *29*(4), 985–1001. https://doi.org/10.1029/93WR00004

Ewing, R., & Hunt, A. (2006). Dependence of the electrical conductivity on saturation in real porous media. *Vadose Zone Journal*, *5*(2), 731–741. https://doi.org/10.2136/vzj2005.0107

Fetter, C. W. (2018). *Applied hydrogeology*. Waveland Press.

Fokker, P. (2001). General anisotropic effective medium theory for the effective permeability of heterogeneous reservoirs. *Transport in Porous Media*, *44*(2), 205–218. https://doi.org/10.1023/A:1010770623874

Friedli, L., Linde, N., Ginsbourger, D., & Doucet, A. (2022). Lithological tomography with the correlated pseudo-marginal method. *Geophysical Journal International*, *228*(2), 839–856. https://doi.org/10.1093/gji/ggab381

Friedli, L., Linde, N., Ginsbourger, D., Visentini, A. F., & Doucet, A. (2023). Inference of geostatistical hyperparameters with the correlated pseudo-marginal method. *Advances in Water Resources*, *173*, 104–402. https://doi.org/10.1016/j.advwatres.2023.104402

Friedman, S. P., & Seaton, N. A. (1998). Critical path analysis of the relationship between permeability and electrical conductivity of three-dimensional pore networks. *Water Resources Research*, *34*(7), 1703–1710. https://doi.org/10.1029/98WR00939

Gelhar, L. W., & Axness, C. L. (1983). Three-dimensional stochastic analysis of macrodispersion in aquifers. *Water Resources Research*, *19*(1), 161–180. https://doi.org/10.1029/WR019i001p00161

Haggerty, R., & Gorelick, S. M. (1995). Multiple-rate mass transfer for modeling diffusion and surface reactions in media with pore-scale heterogeneity. *Water Resources Research*, *31*(10), 2383–2400. https://doi.org/10.1029/95wr10583

Harbaugh, A. W. (2005). MODFLOW-2005, the US Geological Survey modular ground-water model: The ground-water flow process [Software]. *Techniques and Methods*. https://doi.org/10.3133/tm6A16

Hinnell, A., Ferré, T., Vrugt, J., Huisman, J., Moysey, S., Rings, J., & Kowalsky, M. (2010). Improved extraction of hydrologic information from geophysical data through coupled hydrogeophysical inversion. *Water Resources Research*, *46*(W00D40). https://doi.org/10.1029/2008WR007060

Hunt, A. G. (2001). Applications of percolation theory to porous media with distributed local conductances. *Advances in Water Resources*, *24*(3–4), 279–307. https://doi.org/10.1016/S0309-1708(00)00058-0

Hunt, A. G., & Sahimi, M. (2017). Flow, transport, and reaction in porous media: Percolation scaling, critical-path analysis, and effective medium approximation. *Reviews of Geophysics*, *55*(4), 993–1078. https://doi.org/10.1002/2017RG000558

Indelman, P., & Abramovich, B. (1994). A higher-order approximation to effective conductivity in media of anisotropic random structure. *Water Resources Research*, *30*(6), 1857–1864. https://doi.org/10.1029/94WR00077

Johnson, D. L., Koplik, J., & Schwartz, L. M. (1986). New pore-size parameter characterizing transport in porous media. *Physical Review Letters*, *57*(20), 2564–2567. https://doi.org/10.1103/PhysRevLett.57.2564

Katz, A., & Thompson, A. (1986). Quantitative prediction of permeability in porous rock. *Physical Review B*, *34*(11), 8179–8181. https://doi.org/10.1103/PhysRevB.34.8179

Keller, G. V., & Frischknecht, F. C. (1966). *Electrical methods in geophysical prospecting*. Pergamon.

Kemna, A., Vanderborght, J., Kulessa, B., & Vereecken, H. (2002). Imaging and characterisation of subsurface solute transport using electrical resistivity tomography (ERT) and equivalent transport models. *Journal of Hydrology*, *267*(3–4), 125–146. https://doi.org/10.1016/S0022-1694(02)00145-2

Kirkpatrick, S. (1973). Percolation and conduction. *Reviews of Modern Physics*, *45*(4), 574–588. https://doi.org/10.1103/RevModPhys.45.574
Kitanidis, P. K. (1994). The concept of the dilution index. *Water Resources Research*, *30*(7), 2011–2026. https://doi.org/10.1029/94WR00762
Koestel, J., Kemna, A., Javaux, M., Binley, A., & Vereecken, H. (2008). Quantitative imaging of solute transport in an unsaturated and undisturbed soil monolith with 3-D ERT and TDR. *Water Resources Research*, *44*(W12411). https://doi.org/10.1029/2007WR006755
Kowalsky, M. B., Finsterle, S., Peterson, J., Hubbard, S., Rubin, Y., Majer, E., et al. (2005). Estimation of field-scale soil hydraulic and dielectric parameters through joint inversion of GPR and hydrological data. *Water Resources Research*, *41*(W11425). https://doi.org/10.1029/2005WR004237
Laloy, E., Linde, N., & Vrugt, J. A. (2012). Mass conservative three-dimensional water tracer distribution from Markov chain Monte Carlo inversion of time-lapse ground-penetrating radar data. *Water Resources Research*, *48*(W07510). https://doi.org/10.1029/2011WR011238
Le Borgne, T., Dentz, M., & Villermaux, E. (2015). The lamellar description of mixing in porous media. *Journal of Fluid Mechanics*, *770*, 458–498. https://doi.org/10.1017/jfm.2015.117
Linde, N., & Vrugt, J. A. (2013). Distributed soil moisture from crosshole ground-penetrating radar travel times using stochastic inversion. *Vadose Zone Journal*, *12*(1), 1–16. https://doi.org/10.2136/vzj2012.0101
Matheron, G., & De Marsily, G. (1980). Is transport in porous media always diffusive? A counterexample. *Water Resources Research*, *16*(5), 901–917. https://doi.org/10.1029/WR016i005p00901
Milton, G. W., & Sawicki, A. (2003). Theory of composites. Cambridge monographs on applied and computational mathematics. *Applied Mechanics Reviews*, *56*(2), B27–B28. https://doi.org/10.1115/1.1553445
Müller, K., Vanderborght, J., Englert, A., Kemna, A., Huisman, J. A., Rings, J., & Vereecken, H. (2010). Imaging and characterization of solute transport during two tracer tests in a shallow aquifer using electrical resistivity tomography and multilevel groundwater samplers. *Water Resources Research*, *46*(W03502). https://doi.org/10.1029/2008WR007595
Neuman, S. P., & Orr, S. (1993). Prediction of steady state flow in nonuniform geologic media by conditional moments: Exact nonlocal formalism, effective conductivities, and weak approximation. *Water Resources Research*, *29*(2), 341–364. https://doi.org/10.1029/92WR02062
Pollock, D., & Cirpka, O. A. (2012). Fully coupled hydrogeophysical inversion of a laboratory salt tracer experiment monitored by electrical resistivity tomography. *Water Resources Research*, *48*(1). https://doi.org/10.1029/2011WR010779
Pope, S. B. (2001). *Turbulent flows*. Cambridge University Press.
Purvance, D. T., & Andricevic, R. (2000). On the electrical-hydraulic conductivity correlation in aquifers. *Water Resources Research*, *36*(10), 2905–2913. https://doi.org/10.1029/2000WR900165
Renard, P., & De Marsily, G. (1997). Calculating equivalent permeability: A review. *Advances in Water Resources*, *20*(5–6), 253–278. https://doi.org/10.1016/S0309-1708(96)00050-4
Revil, A., Ahmed, A. S., & Matthai, S. (2018). Transport of water and ions in partially water-saturated porous media. Part 3. Electrical conductivity. *Advances in Water Resources*, *121*, 97–111. https://doi.org/10.1016/j.advwatres.2018.08.007
Revil, A., & Cathles, L., III. (1999). Permeability of shaly sands. *Water Resources Research*, *35*(3), 651–662. https://doi.org/10.1029/98WR02700
Rubin, Y. (2003). *Applied stochastic hydrogeology*. Oxford University Press.
Rubin, Y., & Seong, K. (1994). Investigation of flow and transport in certain cases of nonstationary conductivity fields. *Water Resources Research*, *30*(11), 2901–2911. https://doi.org/10.1029/94WR01950
Rücker, C., Günther, T., & Wagner, F. M. (2017). pyGIMLi: An open-source library for modelling and inversion in geophysics [Software]. *Computers & Geosciences*, *109*, 106–123. https://doi.org/10.1016/j.cageo.2017.07.011
Sanchez-Vila, X., Guadagnini, A., & Carrera, J. (2006). Representative hydraulic conductivities in saturated groundwater flow. *Reviews of Geophysics*, *44*(RG3002). https://doi.org/10.1029/2005RG000169
Sen, P. N., & Goode, P. A. (1992). Influence of temperature on electrical conductivity on shaly sands. *Geophysics*, *57*(1), 89–96. https://doi.org/10.1190/1.1443191
Sen, P. N., Scala, C., & Cohen, M. (1981). A self-similar model for sedimentary rocks with application to the dielectric constant of fused glass beads. *Geophysics*, *46*(5), 781–795. https://doi.org/10.1190/1.1441215
Singha, K., Day-Lewis, F. D., & Lane, J. W., Jr. (2007). Geoelectrical evidence of bicontinuum transport in groundwater. *Geophysical Research Letters*, *34*(12). https://doi.org/10.1029/2007GL030019
Singha, K., & Gorelick, S. M. (2005). Saline tracer visualized with three-dimensional electrical resistivity tomography: Field-scale spatial moment analysis. *Water Resources Research*, *41*(W05023). https://doi.org/10.1029/2004WR003460
Slater, L. D., Binley, A., Daily, W., & Johnson, R. (2000). Cross-hole electrical imaging of a controlled saline tracer injection. *Journal of Applied Geophysics*, *44*(2–3), 85–102. https://doi.org/10.1016/S0926-9851(00)00002-1
Slater, L. D., & Lesmes, D. (2002). Ip interpretation in environmental investigations. *Geophysics*, *67*(1), 77–88. https://doi.org/10.1190/1.1451353
Tarantola, A. (2005). In *Inverse problem theory and methods for model parameter estimation* (Vol. 89). SIAM.
Torquato, S., & Haslach, H., Jr. (2002). Random heterogeneous materials: Microstructure and macroscopic properties. *Applied Mechanics Reviews*, *55*(4), B62–B63. https://doi.org/10.1115/1.1483342
Vanderborght, J., Kemna, A., Hardelauf, H., & Vereecken, H. (2005). Potential of electrical resistivity tomography to infer aquifer transport characteristics from tracer studies: A synthetic case study. *Water Resources Research*, *41*(W06013). https://doi.org/10.1029/2004WR003774
Villermaux, E. (2019). Mixing versus stirring. *Annual Review of Fluid Mechanics*, *51*(1), 245–273. https://doi.org/10.1146/annurev-fluid-010518-040306
Visentini, A. F. (2024). An electrical parameter characterizing solute heterogeneity: The mixing factor M [Software]. *Zenodo*. https://doi.org/10.5281/zenodo.11068781
Visentini, A. F., de Anna, P., Jougnot, D., Le Borgne, T., Méheust, Y., & Linde, N. (2021). Electrical signatures of diffusion-limited mixing: Insights from a milli-fluidic tracer experiment. *Transport in Porous Media*, 1–27.
Visentini, A. F., Linde, N., Le Borgne, T., & Dentz, M. (2020). Inferring geostatistical properties of hydraulic conductivity fields from saline tracer tests and equivalent electrical conductivity time-series. *Advances in Water Resources*, *146*, 103–758. https://doi.org/10.1016/j.advwatres.2020.103758
Wen, X.-H., & Gómez-Hernández, J. J. (1996). Upscaling hydraulic conductivities in heterogeneous media: An overview. *Journal of Hydrology*, *183*(1–2), ix–xxxii. https://doi.org/10.1016/S0022-1694(96)80030-8
Wood, B. D. (2009). The role of scaling laws in upscaling. *Advances in Water Resources*, *32*(5), 723–736. https://doi.org/10.1016/j.advwatres.2008.08.015
Yan, S., & Valocchi, A. J. (2020). Flux-corrected transport with MT3DMS for positive solution of transport with full-tensor dispersion. *Ground Water*, *58*(3), 338–348. https://doi.org/10.1111/gwat.12976